J. Fluid Mech. (1999), *vol.* 383, *pp.* 113–142. Printed in the United Kingdom

Direct computation of the sound generated by vortex pairing in an axisymmetric jet

By BRIAN E. MITCHELL†, SANJIVA K. LELE‡ AND PARVIZ MOIN§

Department of Mechanical Engineering, Stanford University Stanford, CA 94305, USA

(Received 29 August 1997 and in revised form 14 October 1998)

The sound generated by vortex pairing in axisymmetric jets is determined by direct solution of the compressible Navier–Stokes equations on a computational grid that includes both the near field and a portion of the acoustic far field. At low Mach number, the far-field sound has distinct angles of extinction in the range of 60°–70° from the jet's downstream axis which can be understood by analogy to axisymmetric, compact quadrupoles. As the Mach number is increased, the far-field sound takes on a superdirective character with the dominant sound directed at shallow angles to the jet's downstream axis. The directly computed sound is compared to predictions obtained from Lighthill's equation and the Kirchhoff surface method. These predictions are in good agreement with the directly computed data. The Lighthill source terms have a large spatial distribution in the axial direction necessitating the introduction of a model to describe the source terms in the region downstream of the last vortex pairing. The axial non-compactness of the quadrupole sources must be adequately treated in the prediction method.

1. Introduction

The use of numerical tools for acoustic predictions, e.g. computational aeroacoustics (CAA), typically relies on various assumptions beyond mere numerical issues. Primary amongst these is the assumption that an aeroacoustic theory such as Lighthill's equation can yield accurate far-field predictions given detailed, but inexact, near-field information. The performance of such predictive methods needs to be carefully considered and validated in flows of interest. For example, it is important to recognize the spatial non-compactness of the acoustic sources and careful consideration is required to model flow–acoustic interaction effects.

In the present study, direct numerical simulations (DNS) are used to directly compute the sound radiated by vortex pairing in the shear layers of axisymmetric round jets. These calculations directly solve the compressible Navier–Stokes equations on a computational domain that includes the near field and a portion of the far field. This type of DNS provides a complete description of the flow field, i.e. both the near-field acoustic source region and the radiated sound are captured in the same computation.

---

† Present address: General Electric Corporate Research and Development Center, PO Box 8, Schenectady, NY 12301, USA.

‡ Also with the Department of Aeronautics and Astronautics.

§ Also with the NASA-Ames Research Center.

We compare the directly computed far-field sound (obtained without an aeroacoustic theory) to predictions obtained with Lighthill's equation (Lighthill 1952) and the Kirchhoff surface method (Pierce 1989, p. 180; Lyrintzis 1994). Such comparisons allow the quantitative accuracy and limitations of these approaches to be assessed. A direct assessment is essential since predictions from theories such as Lighthill's equation rely on various assumptions that are not met in real jets. For instance, a rigorous derivation of Lighthill's equation using matched asymptotic expansions (Crow 1970) requires the assumption of a low-Mach-number compact vortical flow.

While it must be recognized from the outset that the axisymmetric jets considered in the present study differ from fully turbulent jets, it is nevertheless hoped that useful physical insights can be garnered from the consideration of simpler, 'building block' flows and that learning how to predict the sound from the jets considered herein will aid efforts to predict the sound from more complex flows. This belief is motivated by the successful use of DNS of turbulence in canonical flows (Moin & Mahesh 1998) to further the understanding of turbulence physics and to aid turbulence modelling.

Many previous investigators have considered the sound generated by vortex pairing experimentally, see for instance Moore (1977), Kibens (1979), Laufer & Yen (1983), and Bridges & Hussain (1992). Laufer & Yen observed that the far-field sound was highly directive with a strong dependence on the angle from the jets axis. Crighton & Huerre (1990) explained the Laufer & Yen results in terms of the phenomenon of 'superdirectivity' which they showed was a consequence of acoustical non-compactness (see also Huerre & Crighton 1983). Bridges & Hussain, in sharp contrast to Laufer & Yen, observed a striking directivity pattern that was similar to an axisymmetric quadrupole.

In the present study, we consider the sound radiated by vortex pairing in axisymmetric jets which exhaust into a quiescent, stationary medium. The jets considered have a Reynolds based on initial centreline velocity, density, and jet radius, of $Re = \rho_0 U_0 R_0/\mu = 2500$ with Mach numbers based on the ambient speed of sound ($M_j = U_0/c_\infty$) in the range $0.4 \leqslant M_j \leqslant 1.2$. Depending on the initial shear layer thickness, the shear layer of these jets rolls up into vortices which undergo either one or two vortex pairings.

At higher speeds, we observed that vortex pairing does not take place and instead the far-field sound is dominated by intense Mach wave radiation. Mach wave radiation has been observed experimentally in excited jets, see for instance Troutt & McLaughlin (1982). A companion study (Mitchell, Lele & Moin 1997) considers the Mach wave radiation of a higher speed jet ($M_j = 2$) and specifically explores the prediction of Mach wave radiation by different methods.

Our lowest Mach number jet has a directivity pattern similar to the Bridges & Hussain experiment while our highest Mach number jet is superdirective. The directly computed far-field sound is compared to predictions obtained by the solution of Lighthill's equation and with the use of Kirchhoff surfaces. Both prediction methods depend on input from the computations. In the case of Lighthill's equation, the source terms have a large spatial extent that must be dealt with explicitly. Predictions obtained from both methods are in good agreement with the directly computed data.

There are a number of numerical issues that must be carefully addressed in order to perform computations of the sort reported in this paper. These issues include the disparity of length and energy scales, the specification of accurate non-reflecting boundary conditions, the specification of outflow boundary conditions to allow vortical structures to leave the computational domain, and the need to preserve the conservative, non-dispersive nature of the acoustic field. Some of these issues are

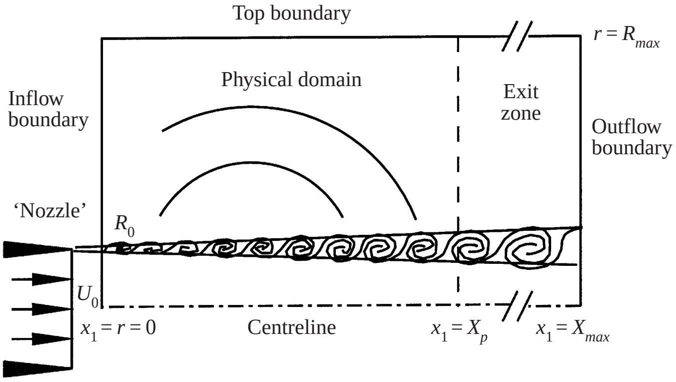

FIGURE 1. Schematic of the computational domain. Note that the sketch is not to scale, in particular $X_{max} \approx 3X_p$.

discussed by Crighton (1993). The disparity of length and energy scales is especially acute for low-Mach-number jets. For the lowest speed jet we considered, a jet with a centreline Mach number of 0.4, the acoustic wavelength of the dominant sound is 23 times larger than the jet radius and the acoustic pressure fluctuations at 40 jet radii away from the jet are 10 000 times smaller than near-field pressure fluctuations.

The previous work of Colonius, Lele & Moin (1994), who directly computed the sound scattered by a single vortex, and Mitchell, Lele & Moin (1995*a*), who computed the sound radiated by co-rotating vortices, has clearly demonstrated that our numerical schemes are capable of computing the sound generated by aerodynamic motions. Furthermore, the recent computations of the sound radiated by a two-dimensional mixing layer (Colonius, Lele & Moin 1995*a*,*b*; Colonius, Lele & Moin 1997) have demonstrated that our numerical schemes and boundary conditions may be used to compute the sound radiated by free shear flows.

In § 2, we summarize the numerical procedure, and in § 3, our results are presented. In § 4, the solution procedure for Lighthill's equation is detailed and the predictions of Lighthill's equation are compared to the directly computed far-field sound. In § 5, the application of a Kirchhoff surface for predicting far-field sound is discussed, and predictions are compared to the directly computed sound. Conclusions are offered in § 6.

2. Numerical method

A schematic of the computational domain is shown in figure 1; the computational domain includes the region $0 \leqslant x_1 \leqslant X_{max}$ and $0 \leqslant r \leqslant R_{max}$, where x_1 is the axial coordinate and r is the radial coordinate. Only the region $0 \leqslant x_1 \leqslant X_p$ is considered to contain physically meaningful data since the region $X_p < x_1 \leqslant X_{max}$ is an exit zone constructed to allow large-scale vortices to exit the computational domain without reflecting significant acoustic disturbances back into the region of interest. The inflow boundary, $x_1 = 0$, is considered to be located a short distance downstream of a (hypothetical) nozzle. No attempt is made to model the effects of the nozzle and flow delivery system on the near-field aerodynamics or the far-field sound; nozzle scattering effects such as studied by Crighton (1972) are ignored.

The domain is discretized with a structured mesh containing N_x points in the x_1-direction and N_r points in the radial direction. In the axial direction, there are

$N_{x_p} < N_x$ points in the physical part of the domain. The velocity in the axial direction is u and velocity in the radial direction is v_r.

The governing equations are the axisymmetric, compressible Navier–Stokes equations together with the ideal gas law, constant viscosity and thermal conductivity, unity Prandtl number, Stokes hypothesis to eliminate the bulk viscosity, and ratio of specific heats of 1.4. Time advancement is via the fourth-order-accurate Runge–Kutta algorithm and spatial derivatives are evaluated using fourth-order-accurate Padé schemes, see for instance Lele (1992). This combination of temporal and spatial schemes has minimal dissipation and excellent dispersion properties and allows for accurate propagation of acoustic waves. At the centreline, the coordinate singularity is avoided by solving the Navier–Stokes equations in Cartesian coordinates (Thompson, Warsi & Mastin 1985, p. 148) using eighth-order-accurate explicit finite differences to evaluate spatial derivatives.

First-order boundary conditions due to Giles (1990) and discussed by Colonius, Lele & Moin (1993) are posed on subsonic portions of inflow boundary and on the top boundary. Zeroth-order boundary conditions are used on the supersonic portions of the inflow boundary and on the entire outflow boundary. We found that the damping terms required by Colonius *et al.* (1993) were not needed in the present computations. Inside the exit zone, the grid is stretched significantly in the axial direction and filtering is performed to attenuate the vorticity and to remove any acoustic waves generated by the grid stretching, see Colonius *et al.* (1993) for more details.

Initial conditions are specified using the solution of the parabolic boundary layer starting with a hyperbolic tangent profile at $x_1 = -5R_0$. The boundary layer equations are solved starting at $x_1 < 0$ to ensure that spatial transients have decayed by $x_1 = 0$. The momentum thickness, defined as

$$\delta_2(x_1) = \int_0^\infty \left(\frac{u(x_1,r)}{u(x_1,0)}\right)\left(1 - \frac{u(x_1,r)}{u(x_1,0)}\right) \mathrm{d}r, \tag{2.1}$$

of the hyperbolic tangent profile at $x_1 = -5R_0$ is specified such that the momentum thickness at $x_1 = 0$ has some desired value ($\delta_2(0) = 0.1R_0$ or $0.05R_0$ in the current study). In addition to the hyperbolic tangent velocity profile at $x_1 = -5R_0$, the Crocco–Busemann relationship is used to establish the initial temperature profile given the requirement that the centreline static temperature is the same as the ambient static temperature, see Michalke (1984). Note that the profile at $x_1 = -5R_0$ is not isothermal since the Crocco–Busemann relationship predicts a rise in static temperature in the shear layer due to viscous heating effects.

In order to induce the roll-up and pairing of vortex rings, the flow at the inflow boundary is perturbed in a time-periodic manner at the fundamental frequency and its first few subharmonics where the fundamental frequency, f_0, is defined as the frequency at which disturbances acquire the largest spatial amplification rate for the jet velocity profile at $x_1 = 0$ as computed using inviscid, parallel flow linear stability theory.

Because of the periodic inflow forcing and a lack of spectral broadening due to the axisymmetry and low Reynolds number, the jet approaches a periodic state and it is thus convenient to decompose the computational data into discrete frequencies using Fourier transforms, e.g.

$$f(t) = \sum_n \hat{f}(\omega_n)\,\mathrm{e}^{-\mathrm{i}\omega_n t}. \tag{2.2}$$

Parameter	$M_j = 0.4$ (thick)	0.8 (thick)	1.2 (thick)	0.8 (thin)
δ_2/R_0	0.10	0.10	0.10	0.05
St_0	0.22	0.21	0.18	0.34
X_p/R_0	70	70	70	60
R_{max}/R_0	80	80	80	60
N_{x_p}	1557	1557	1557	2668
N_r	292	415	492	652
$\Delta x_1/R_0$	0.045	0.045	0.045	0.0225
$\Delta r_{min}/R_0$	0.030	0.030	0.030	0.015
$\Delta r_{max}/R_0$	0.648	0.306	0.231	0.179

TABLE 1. Flow and grid parameters.

Use of Fourier decompositions also simplifies the solution of Lighthill's equation and the use of a Kirchhoff surface.

Further details on the numerical algorithm may be found in Mitchell, Lele & Moin (1995*b*).

2.1. *Flow and grid parameters*

Using the numerical method described above, four cases were run on a Cray-YMP-C90 supercomputer. The flow and grid parameters for these cases are summarized in table 1. The primary difference is the Mach number, based on the centreline velocity at $x_1 = 0$ and the speed of sound in the ambient fluid ($M_j = U_0/c_\infty$), and the initial momentum thickness ($\delta_2(x_1 = 0)$). All of the cases are excited at the fundamental frequency (f_0) and first few subharmonics. The Strouhal number of the fundamental frequency is defined as $St_0 = f_0R_0/U_0$. All of the cases are for $Re = \rho_0U_0R_0/\mu = 2500$. The jets exhaust into a stationary medium.

The first three cases are for $\delta_2(x_1 = 0) = 0.1R_0$ with different initial centreline Mach numbers: $M_j = 0.4$, 0.8, and 1.2. The jets are excited at the fundamental and first two subharmonic frequencies. In the radial direction, the number of grid points is increased with increasing Mach number due to the decrease in the acoustic wavelength, λ, which can be estimated by $\lambda/R_0 = 1/(M_jSt)$. These cases will be referred to by their Mach number, e.g. the '$M_j = 0.4$ jet'. Collectively, these cases will also be referred to as the 'thick shear layer jets' to distinguish them from the fourth case considered. The $M_j = 1.2$ supersonic jet is perfectly expanded in order to avoid shock noise.

The fourth case is for $\delta_2(x_1 = 0) = 0.05R_0$, and $M_j = 0.8$. The jet is excited at the fundamental and three subharmonic frequencies. This case will be referred to as the 'thin shear layer, $M_j = 0.8$ jet'.

The radial grid spacing was chosen to place approximately 12 points per vorticity thickness (approximately $4\delta_2$ at $x_1 = 0$) in the near field and approximately 10 points per acoustic wavelength for acoustic waves at the $2f_0$ frequency. The region of grid stretching is centred around $r = 5R_0$ and the grid is stretched slowly. Tests with simple sound sources verified that the propagation of acoustic waves was not affected by the region of grid stretching. In the physical part of the axial grid, $0 < x_1 < X_p$, the axial grid spacing is chosen to place approximately 9 points per vorticity thickness. The exit zone is sized such that $X_{max} - X_p = 100R_0$ and $N_x - N_{x_p} = 400$. The ratio of minimum to maximum axial grid spacing in the exit zone is 50.

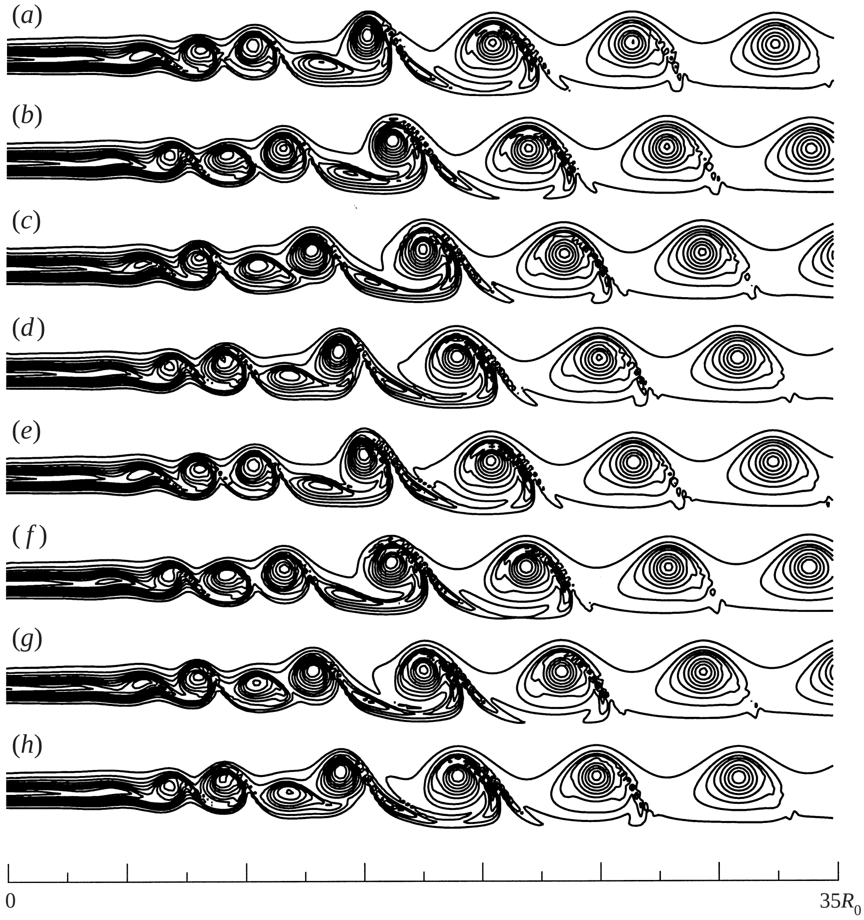

FIGURE 2. Evolution of vorticity for the $M_j = 0.4$ jet showing equally spaced intervals in time during one period of the second sub-harmonic frequency, i.e. time is increasing from plots (*a*) to (*h*) with spacing $\Delta t = f_0/4$. The contour levels range from 0 to $2.8U_0/R_0$ with increment $0.28U_0/R_0$. The radial coordinate has been magnified by a factor of 2. Only half of the streamwise extent of the computational domain is shown.

3. Results

The response of the jets to the inflow excitation is to roll up into discrete vortices which subsequently pair. In the case of the thick shear layer jets, only a single vortex pairing takes place, see for instance figure 2. The evolution for the other thick shear layer jets is similar; however, the locations of the vortex roll-up and pairing move further downstream as the Mach number is increased. The delay of the vortex roll-up and pairing are in accordance with linear stability theory which shows that the growth rates of disturbances decreases as the Mach number is increased, see for instance Michalke (1984). The thin shear layer $M_j = 0.8$ jet undergoes two vortex pairings, see figure 3. After the last vortex pairing, the resulting vortices convect downstream at speed $\approx 0.64M_j$ for the thick shear layer jets, and speed $\approx 0.69M_j$ for the thin shear layer jet; viscosity acts to reduce the peak level of vorticity.

The development of the momentum thickness is shown in figure 4. For all cases, the momentum thickness is observed to have a step-like increase in the region of the

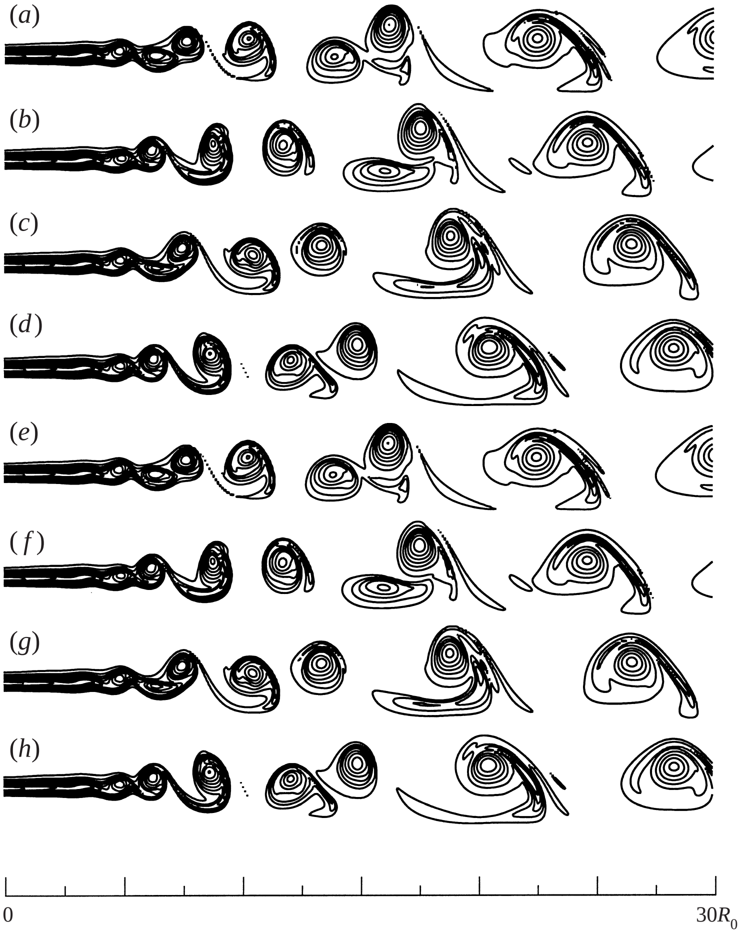

FIGURE 3. Evolution of vorticity for the thin shear layer, $M_j = 0.8$ jet showing equally spaced intervals in time during one period of the fourth subharmonic frequency, i.e. time is increasing from plots (*a*) to (*h*) with spacing $\Delta t = f_0/8$. The contour levels range from 0 to $2.88U_0/R_0$ with increment $0.288U_0/R_0$. The radial coordinate has been magnified by a factor of 2. Only half of the streamwise extent of the computational domain is shown.

vortex pairings. For the thick shear layer jets, the start of the increase is delayed as the Mach number is increased and the increase occurs more gradually. Unlike the vortex pairing, the vortex roll-up does not have any discernible effect on the growth of the momentum thickness. Experimental measurements of jets and mixing layers also find a step-like increase in the momentum thickness in regions of vortex pairing, see for instance Ho & Huang (1983) and Laufer & Zhang (1983).

Fourier transforms of near- and far-field flow quantities showed that the jets approach a time-periodic state. In particular, it was found that both the near and far fields are dominated by 'even frequencies' which are defined by $(n/4)f_0$ for the thick shear layer jets and $(n/8)f_0$ for the thin shear layer jets, where n is even. These frequencies represent combinations and multiples of the vortex roll-up and pairing frequencies. (For the thin shear layer, $M_j = 0.8$ jet, there are persistent cycle-to-cycle variations; however, we found that accurate Fourier transforms could be computed

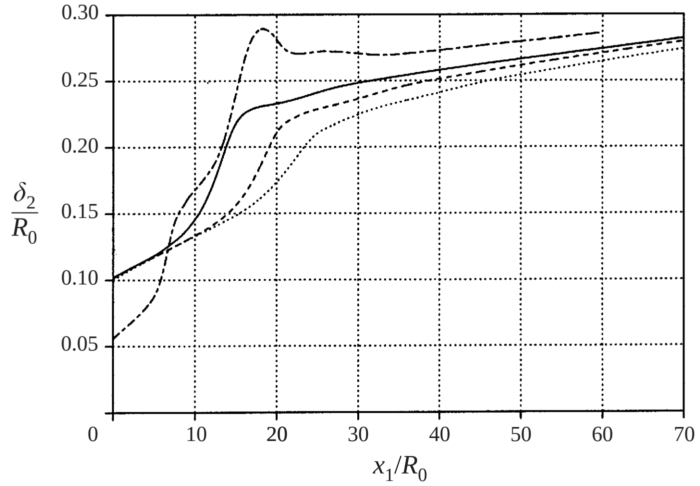

FIGURE 4. The axial growth of the momentum thickness for the jets: ——, $M_j = 0.4$; - - - -, $M_j = 0.8$; ········, $M_j = 1.2$; and — — —, thin shear layer $M_j = 0.8$.

by averaging the results over a few periods of data, see Mitchell *et al.* 1995*b* for more details.)

The growth of axial velocity disturbances at the frequencies which corresponds to the vortex roll-up and pairing are shown in figure 5 for the thick shear layer jets. There are several features to note. First, the largest disturbance is at the first subharmonic frequency which saturates where the step-like increase in the momentum thickness is complete. The correspondence of the saturation location and the completion of the step-like increase was also observed by Ho & Huang (1982) who denoted the location of saturation the 'vortex-merging' location. Second, disturbances at the fundamental frequency are seen to saturate in the region of vortex roll-up, decrease, and then to saturate, i.e. peak, again during vortex pairing. Multiple saturations have been observed by other investigators, see for instance Colonius *et al.* (1995*b*) and Laufer & Zhang (1983). Third, the saturation amplitude of the disturbances decreases slightly as the Mach number is increased. The saturation location of the first subharmonic frequency can be used to denote the 'vortex-pairing' location. This location is at $x_1 = 15.7R_0$ for the $M_j = 0.4$ jet; $x_1 = 21.5R_0$ for the $M_j = 0.8$ jet; and $x_1 = 25.6R_0$ for the $M_j = 1.2$ jet.

Figure 6 shows the growth of disturbances for the thin shear layer, $M_j = 0.8$ jet. Disturbances at the first and second subharmonic frequencies saturate where the step-like increase in the momentum thickness is complete. Although their spatial evolution is not shown, there are other frequencies present in the near field with disturbance levels similar to, but generally smaller than, that of the fundamental frequency. For instance, disturbances at the $\frac{3}{4}f_0$ frequency saturate in the region of the second vortex pairing with peak amplitude similar to the peak amplitude for disturbances at the fundamental frequency. The vortex pairing locations, as measured by the saturation locations of the first and second subharmonics, are at $x_1 = 9.6R_0$ and $x_1 = 18.0R_0$.

Note that disturbances at all frequencies decrease only slightly from their 'saturation levels' before the outflow of the computational domain. This has important implications for acoustic predictions via Lighthill's equation, see § 4.1 for more details.

Figure 7 shows an instantaneous picture of the near-field vorticity and far-field dilatation, $\Theta = \nabla \cdot \boldsymbol{u}$. For all the jets, the dominant sound is generated in the regions

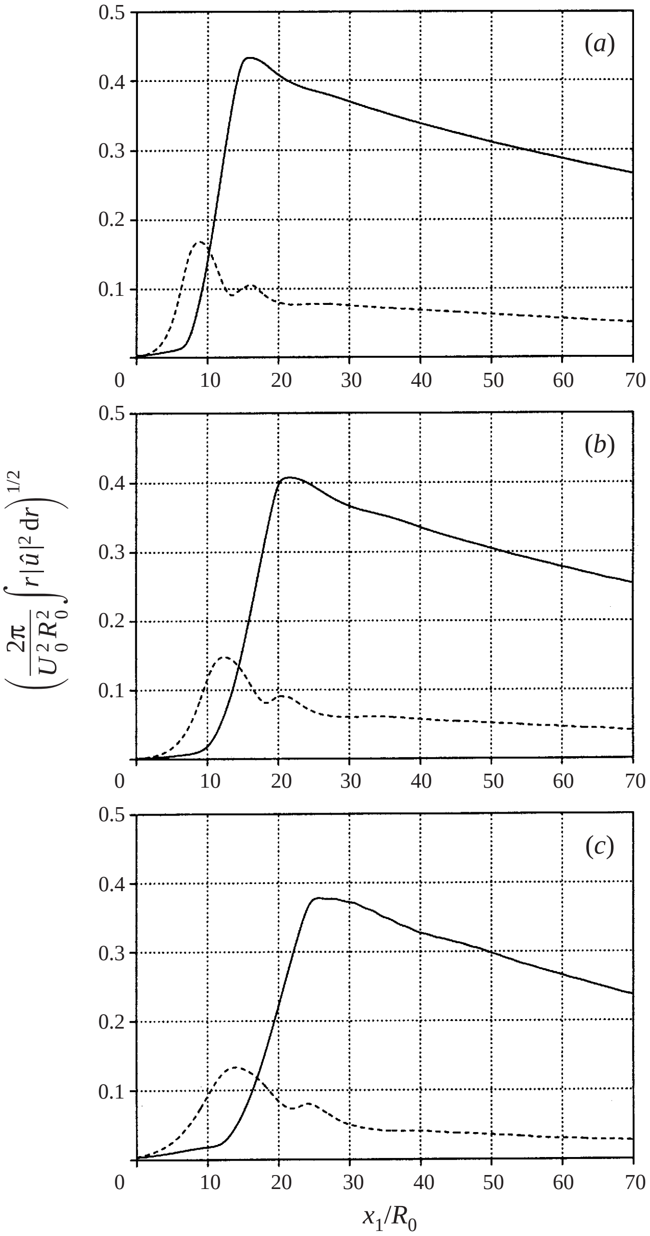

FIGURE 5. Growth of axial velocity disturbances, $\hat{u}$, at various frequencies for the jets (*a*) $M_j = 0.4$, (*b*) $M_j = 0.8$, (*c*) $M_j = 1.2$ jets. The curves are for: ———, $\frac{1}{2}f_0$; and - - - -, f_0.

of the vortex pairing(s). As the Mach number is increased for the thick shear layer jets, the sound becomes concentrated at shallow angles to the jet's downstream axis. Fourier transforms of the far field verified that only multiples and combinations of the inflow forcing frequencies are present there; there is no observable Doppler shift in frequency. Evidently the sound sources are stationary, a conclusion that was also reached by Kibens (1979), Laufer & Yen (1983), and Bridges & Hussain (1992) in their experiments with vortex pairing in low-Mach-number excited jets. These Fourier

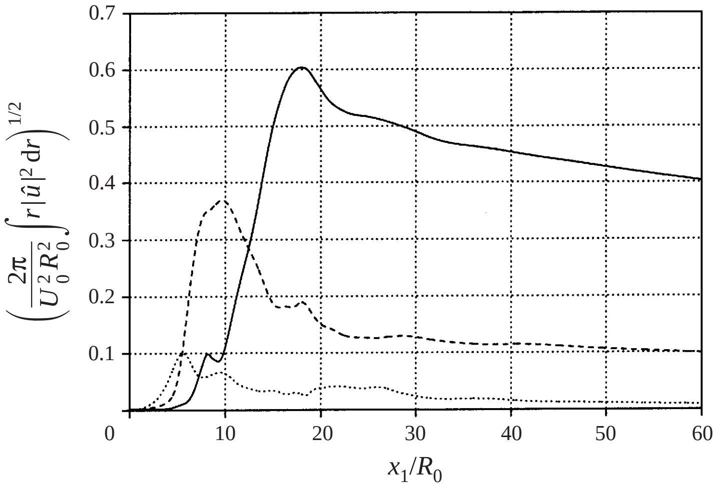

FIGURE 6. Growth of axial velocity disturbances, $\hat{u}$, at various frequencies for the thin shear layer $M_j = 0.8$ jet: ——, $\frac{1}{4}f_0$; ----, $\frac{1}{2}f_0$ and ········, f_0.

transforms also revealed that sound at the 'odd frequencies' was at least 20 dB less than sound at the 'even frequencies'.

In order to discuss the directivity of the far-field sound, we consider an observer located on a sphere of radius x centred on the x_1-axis at $x_1 = x_s$. Let θ be the angle made by the observer location with the downstream x_1-axis. The sound field is axisymmetric about the x_1-axis but depends on θ. The value of x_s used for each frequency and Mach number is tabulated in table 2 and represents an estimate of the location of the apparent sound source which was obtained by examining two-dimensional contour plots, similar to figure 7, of the sound at each frequency, see Mitchell *et al.* (1995*b*). For frequencies at which there is more than one apparent sound source, x_s was estimated based on the dominant source.

With the exception of the second subharmonic frequency ($f_0/4$) for the thick shear layer jets which is observed to be dominated by the inflow forcing, the sound sources are located in the region where the vortex pairing(s) takes place. For the thin shear layer $M_j = 0.8$ jet which has two vortex pairings, sound at the first subharmonic frequency appears to be radiated from the region of the first vortex pairing, and sound at the second harmonic frequency appears to be radiated from the region of the second vortex pairing. For frequencies which do not directly correspond to vortex pairing events, there is no evident trend in the location of the sources other than the fact that the sound is radiated from the region of the vortex pairings.

The directivity of the sound at individual frequencies for the thick shear layer jets is shown in figure 8. The large values of the dilatation at very small angles are caused by the placement of the observation point in the near field and should not be interpreted as sound. Mitchell *et al.* (1995*b*) document that these fluctuations are associated with the instabilities waves.

For the $M_j = 0.4$ jet, shown in figure 8(*a*), the dominant frequency of the radiated sound is the first subharmonic frequency. This is not surprising since this is the frequency of the vortex pairing and the frequency which contains the most energy in the near field, see figure 5. We also note that several of the frequencies, including the first subharmonic and fundamental frequencies, have an 'angle of extinction' or local minimum in the sound level at around 60°–70° from the downstream jet axis. Bridges

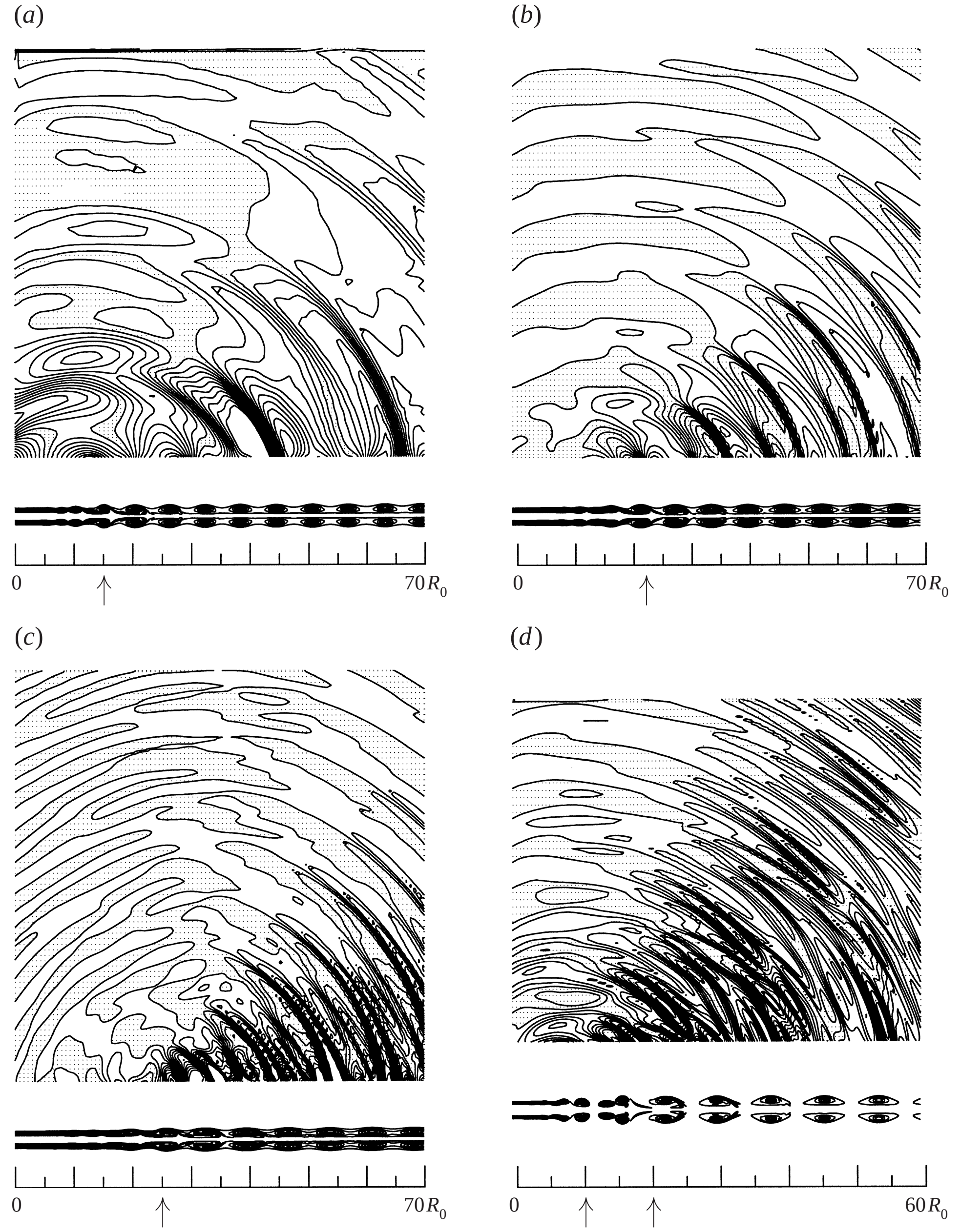

FIGURE 7. Instantaneous near-field vorticity and far-field dilatation fields: (*a*) $M_j = 0.4$ jet, (*b*) $M_j = 0.8$ jet, (*c*) $M_j = 1.2$ jet, and (*d*) thin shear layer $M_j = 0.8$ jet. The contours of the far-field dilatation are: (*a*) min/max $\pm 3 \times 10^{-6}$, incr. 3×10^{-7}; (*b*) min/max $\pm 1 \times 10^{-4}$, incr. 1×10^{-5}; (*c*) min/max $\pm 1 \times 10^{-3}$, incr. 1×10^{-4}. and (*d*) min/max $\pm 4 \times 10^{-4}$, incr. 4×10^{-5}. Shaded regions denote negative dilatation. The arrow denotes the vortex pairing locations.

& Hussain (1992) measured the axisymmetric sound generated by vortex pairing in a jet and observed an angle of extinction at 65°. To the best of our knowledge, no other experimental study has looked for the angle of extinction.

For the $M_j = 0.4$ jet, the acoustic wavelengths of the first subharmonic and

Frequency	$M_j = 0.4$ (thick)	0.8 (thick)	1.2 (thick)	0.8 (thin)
$\frac{1}{4}f_0$	0	0	0	14
$\frac{1}{2}f_0$	11	19	17	7
$\frac{3}{4}f_0$				11
f_0	17	19	17	7
$\frac{5}{4}f_0$				14
$\frac{3}{2}f_0$	19	19	18	9
$\frac{7}{4}f_0$				15
$2f_0$	14	19	20	17

TABLE 2. Apparent source locations, x_s/R_0, for various frequencies. In cases where sound appears to be generated from more than one location, only the dominant source location is indicated.

fundamental frequencies are $22.7R_0$ and $11.4R_0$, respectively which is large compared to the radius of the jet and we would anticipate that the sound sources are acoustically compact. If this is the case, then the existence of the angle of extinction can be understood by considering theoretical results for axisymmetric point quadrupoles,

$$\nabla^2_{(y)}\hat{p} + \left(\frac{\omega}{c_\infty}\right)^2 \hat{p} = \frac{\partial^2}{\partial y_i\,\partial y_j}[\hat{Q}_{ij}\delta(y)], \tag{3.1}$$

where $\hat{p}$ is the temporal Fourier transform of the far-field pressure. The sound from this source contains contributions from two terms (Morse & Ingard 1968, p. 347): (i) a quadrupole term with uniform directivity proportional to the trace of $\hat{Q}_{ij}$ and (ii) a quadrupole term that is multiplied by the spherical harmonic, $Y_2(\theta)$,

$$Y_2(\theta) = \tfrac{1}{4}(3\cos(2\theta) + 1). \tag{3.2}$$

If $\hat{Q}_{ij}$ is trace free then the first term is zero and the axisymmetric quadrupole has an angle of extinction at 55°. Bridges & Hussain argued based on Möhring's equation (Möhring 1978) that the first term is zero and sought to explain why their experimentally measured angle of extinction was different from 55°. However, the source tensor in Lighthill's equation is not trace free and the influence of the first term is seen where the contribution of the other term is small, i.e. near $\theta = 55°$; its primary effect is to shift the observed angle of extinction. Thus angles of extinction are not expected to be exactly at 55°.

Returning to figure 8, we observe that as the Mach number is increased the first subharmonic frequency remains the dominant frequency of far-field sound. However, the directivity of the first subharmonic becomes increasingly dependent on the angle θ with the peak sound concentrating towards shallower angles with the downstream jet axis. This trend towards strong dependence on θ is not limited to the first subharmonic and is present for all the frequencies shown in figure 8. Recognizing that as the Mach number is increased, the acoustic wavelengths decrease and the sound sources become non-compact, we explain this trend by reference to the work of Crighton & Huerre (1990) who demonstrated that non-compactness in the axial direction leads to the possibility of superdirective sound sources, i.e. sound sources with a preferred directivity at shallow angles to the jet axis and an exponential

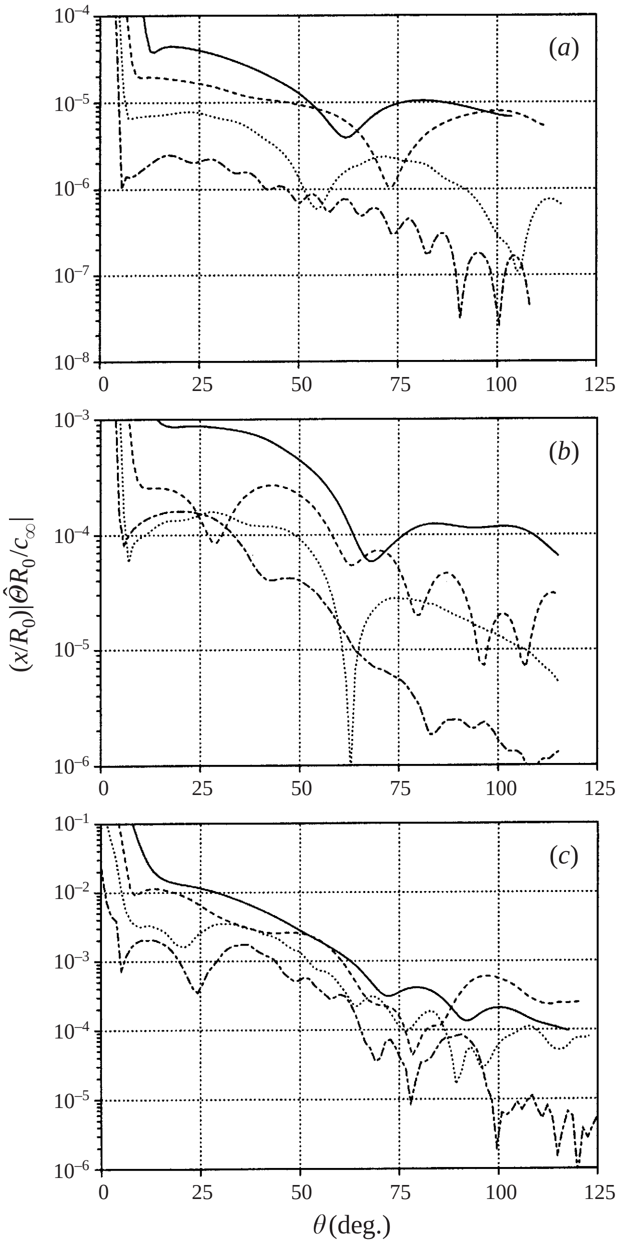

FIGURE 8. The magnitude of the Fourier transform of the far-field dilatation for various frequencies at a distance of $x = 40R_0$ from the apparent source location, x_s, measured versus angle with the downstream axis for the jets (*a*) $M_j = 0.4$, (*b*) $M_j = 0.8$, and (*c*) $M_j = 1.2$. The curves are for: ——, $\frac{1}{2}f_0$; ----, f_0; ········, $\frac{3}{2}f_0$; and — — —, $2f_0$.

dependence on $\cos(\theta)$. We have verified for the $M_j = 1.2$ jet that the far-field sound has an exponential dependence on $\cos(\theta)$ at low angles – in fact, the directivity is well approximated by $e^{6\cos(\theta)}$ for $\theta < 70°$. Laufer & Yen (1983) observed superdirective sources in their low-Mach-number jet noise experiments.

Crighton & Huerre (1990) modelled the source region as a sinusoidal carrier wave

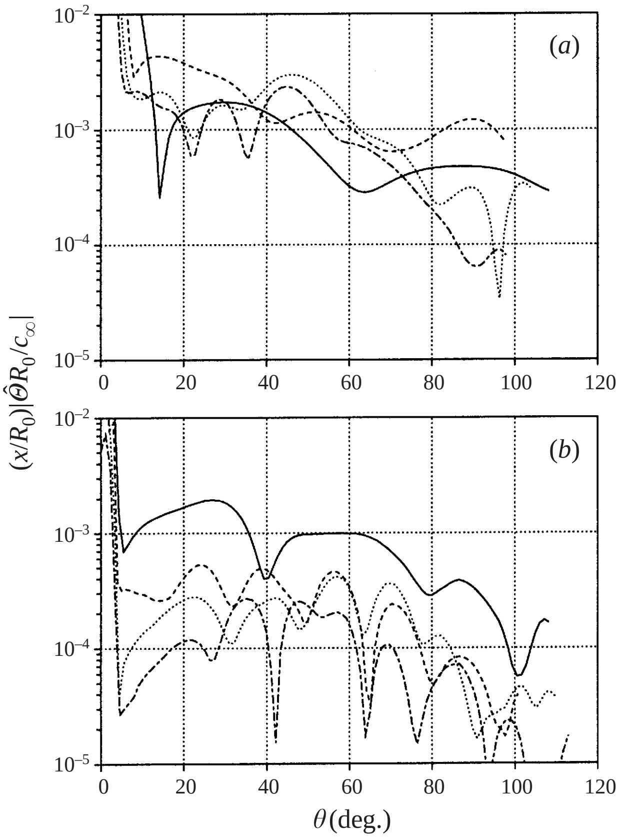

FIGURE 9. As figure 8 but for the thin shear layer, $M_j = 0.8$ jet. In plot (a) the curves are for: ———, $\frac{1}{4}f_0$; - - - -, $\frac{1}{2}f_0$; ········, $\frac{3}{4}f_0$; and — - —, f_0. In plot (b) the curves are for: ———, $\frac{5}{4}f_0$; - - - -, $\frac{3}{2}f_0$; ········, $\frac{7}{4}f_0$; and — - —, $2f_0$.

modulated by a Gaussian envelope function. In the present case, the sound sources are better modelled by a carrier wave that is modulated by an exponential growth followed by a gradual decay, see figures 5, 10 and 11. As the Mach number is increased, the spatial frequency of the carrier wave is nearly unchanged, and the vortices which form are observed to convect at a fixed fraction of the initial centreline velocity independent of M_j. The modulating function is also only slightly modified. However as the Mach number is increased, the acoustic wavelength is reduced and, as a result, the acoustic source region becomes less compact and the trend towards superdirective sound is not surprising. Examination of a model problem based on the sources observed in this study also showed this trend towards superdirectivity. We stress that the key feature is the reduction in the acoustic wavelength implied by the increased Mach number and not the effect of the increased Mach number on the near-field flow structure.

Examination of two-dimensional contour plots for the $M_j = 1.2$ jet revealed that for all the frequencies considered, the sound in the relatively quiet portion of the far field, i.e. $\theta > 90°$, was being radiated from a second sound source located downstream of the vortex pairing in the region $40R_0 < x_1 < 50R_0$. Also, examination of the fundamental frequency of the $M_j = 0.8$ jet shows evidence of a weak second sound source that is either due to the inflow forcing or perhaps due to the vortex roll-up.

These secondary sound sources help explain the oscillations shown in figure 8 for large θ. See Mitchell *et al.* (1995*b*) for more details. Similarly, it was observed that the sound at $2f_0$ for the $M_j = 0.4$ jet is contaminated by weak reflections from the exit zone. These reflections are evidenced by the oscillations present in figure 8(*a*). This was the only case for which we observed reflections from the exit zone.

The directivity of the sound at individual frequencies for the thin shear layer $M_j = 0.8$ jet is shown in figure 9. The far-field directivity is quite complicated, for instance at the $\frac{3}{2}f_0$ frequency, there are six local minima. Overall, the sound levels are roughly an order of magnitude larger than were found in the thick shear layer, $M_j = 0.8$ jet, see figure 8(*b*). Our estimates for the location of the primary sound sources for the thin shear layer jet are in the range of $7R_0$–$17R_0$, see table 2. Except for the first and second subharmonic frequencies, sound appears to be generated from the region of *both* vortex pairings; however, the primary source location is typically in the region of the first vortex pairing. Different regions of the far field seem to contain sound that was radiated from the different sources. For example we observed that at the $\frac{3}{2}f_0$ frequency, sound at small θ appears to come from the region of the second vortex pairing, the sound at higher angles appears to come from the first vortex pairing, and the sound at $\theta > 90°$ comes from the region of the second vortex pairing. The existence of two source locations, from which sound can destructively interfere, coupled with the expected quadrupole behaviour of each source gives rise to the multiple peaks and minima in the directivity. See Mitchell *et al.* (1995*b*) for more details on the source locations.

Finally, we note that although linear stability theory shows that, for very low frequencies, instabilities waves with supersonic phase velocities are possible for the $M_j = 1.2$ jet, we did not observe the intense Mach waves associated with such instability waves, see for instance Tam & Hu (1989). Mitchell *et al.* (1995*b*, 1997) present computational results for a $M_j = 2$ jet where Mach wave radiation dominates the far field.

4. Lighthill's equation

Lighthill (1952) rearranged the exact continuity and momentum equations to derive what has become known as Lighthill's equation:

$$\frac{\partial^2 \rho'}{\partial t^2} - c_\infty^2 \nabla_{(y)}^2 \rho' = \frac{\partial^2}{\partial y_i \, \partial y_j} T_{ij}(\boldsymbol{y}; t). \tag{4.1}$$

The Lighthill stress tensor, T_{ij}, is given by

$$T_{ij} = \rho u_i u_j + (p' - c_\infty^2 \rho')\delta_{ij} - \tau_{ij} \ , \tag{4.2}$$

where τ_{ij} is the viscous stress, and the prime superscript denotes a fluctuating quantity, e.g. $\rho' = \rho - \rho_\infty$. As expressed, equation (4.1) is an exact, single equation involving five flow variables. Approximation is introduced when the left-hand side is inverted to solve for ρ' in terms of an independently specified right-hand side. When used in this manner, Lighthill's equation provides a prediction for ρ' based on prescribed $T_{ij}(\boldsymbol{y}; t)$ (which we approximate as $T_{ij} = \rho u_i u_j + \left(p' - c_\infty^2 \rho'\right) \delta_{ij}$).

It is the goal of this section to explore the ability of Lighthill's equation to predict the computations of sound radiated by the jet presented in § 3. Before discussing the solution of Lighthill's equation in § 4.2, we discuss the problem of extensive source terms in § 4.1. Predictions obtained using source terms computed from the simulations are compared to the directly computed data in § 4.3.

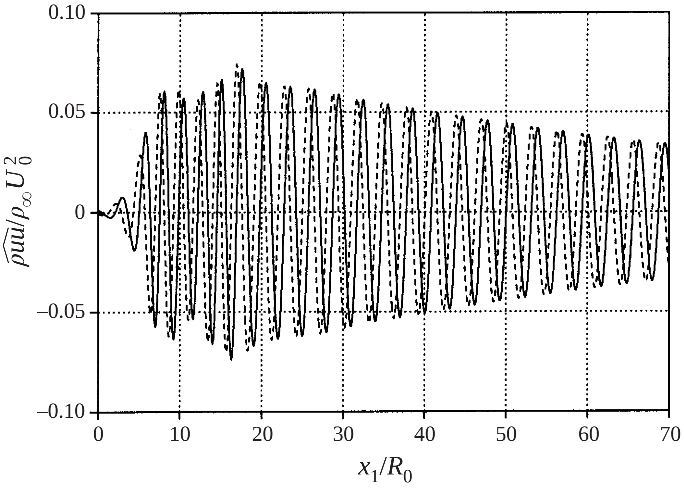

FIGURE 10. The real (———) and imaginary (– – – –) parts of the Fourier transform of a component of the Lighthill source term, $\rho uu/(\rho_\infty U_0^2)$, at $r = R_0$ for the fundamental frequency of the $M_j = 0.4$ jet. Other frequencies and Mach numbers show similar behaviour for $x_1 > 40R_0$.

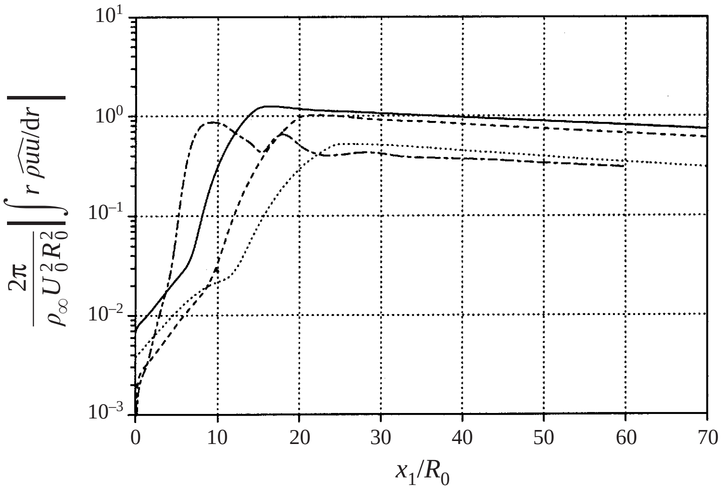

FIGURE 11. The magnitude of the Fourier transform of a component of the Lighthill source term, $\rho uu/(\rho_\infty U_0^2)$, integrated in the radial direction at the first subharmonic frequency for the jets: ———, $M_j = 0.4$; – – – –, $M_j = 0.8$; ········, $M_j = 1.2$ and — — —, thin shear layer $M_j = 0.8$.

Before proceeding, a notational issue needs to be addressed. When dealing with Green's function solutions of the wave equation, such as considered both here and in § 5, a distinction needs to be made between source and observer coordinates. The observer coordinates will be denoted by $\boldsymbol{x}$ and have cylindrical coordinate components (x_1, r). The source coordinates will be denoted by $\boldsymbol{y}$ with cylindrical components (y_1, σ, ϕ). Since we consider only axisymmetric acoustic fields, the azimuthal angle of the observer coordinate system has been suppressed.

4.1. *Extensive source region*

Before discussing the solution of Lighthill's equation, a problematic feature of the Lighthill source terms needs to be considered. This feature is illustrated in figure

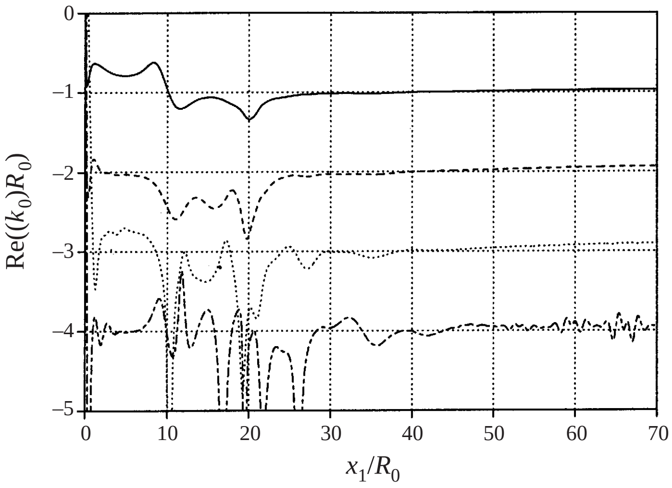

FIGURE 12. The real part of $k_0 = -\mathrm{i}\partial\widehat{\rho uu}/\partial x_1/\widehat{\rho uu}$ evaluated at $r = R_0$ for the $M_j = 0.8$ jet. The curves are for ——, $\frac{1}{2}f_0$; - - - -, f_0; ·······, $\frac{3}{2}f_0$; and – – –, $2f_0$.

10, which shows the real and imaginary parts of the Fourier transform of ρuu at the fundamental frequency for the $M_j = 0.4$ jet, and in figure 11, showing the axial development of the magnitude of the radial integral of ρuu at the first subharmonic frequency for each jet. Evident in these plots is the fact that the source terms decay quite slowly after the vortex pairing(s) and are still significant at the exit of the computational domain. Mankbadi, Hayer & Povinelli (1994) also observed extensive Lighthill sources in their simulation of the near field of a supersonic jet. Note that at the inflow, the source terms are quite small (at least two orders of magnitude smaller than their peak values). The slow decay of the source terms is an artifact of the axisymmetric jets considered here and we do not expect the decay to be so slow when considering turbulent jets.

Because the source terms are still large at the exit of the computational domain, predictions of Lighthill's equation will contain spurious sound waves generated by the sudden termination of the source terms at $x_1 = X_p$. We avoid this problem by observing that downstream of the vortex pairing, say for $x_1 > x_m$, the source terms can be approximated by

$$\hat{T}_{ij}(x_1, r; \omega) = \hat{f}_{ij}(r; \omega)\, \mathrm{e}^{\mathrm{i}k_0(x_1 - x_m)} \tag{4.3}$$

where k_0 is a complex wavenumber with positive imaginary part. Thus the source field is broken into two regions. For $0 \leqslant x_1 < x_m$ (the active region), T_{ij} is evaluated from the simulation and for $x_1 \geqslant x_m$ (the passive region), T_{ij} is evaluated using equation (4.3) where $\hat{f}_{ij}$ and k_0 are evaluated from the simulation data at $x_1 = x_m$.

The accuracy of our model for T_{ij}, (4.3), is checked in figure 12 where the axial variation of k_0 for the $M_j = 0.8$ jet is shown. The wavenumber, k_0, was computed via

$$k_0(x_1, r) = -\mathrm{i}\frac{\partial\widehat{\rho uu}/\partial x_1}{\widehat{\rho uu}} . \tag{4.4}$$

We observed that sufficiently far downstream of the inflow, the real part of k_0 becomes only a weak function of x_1. Although not shown, k_0 is virtually independent of r. Note that the independence of k_0 from x_1 degrades with increasing frequency; this is especially true for the higher frequencies of the $M_j = 1.2$ jet and the thin shear layer $M_j = 0.8$ jet. The imaginary part of k_0 does not, in general, become independent of x_1 and r. Fortunately, the imaginary part of k_0 is much smaller than the real part of k_0, and the overall solution is not very sensitive to its value.

The wavenumber computation, (4.4), is based on the ρuu component since this is the largest. Computations of k_0 using other components of the source term gave nearly identical results for the real part of k_0 (in the region downstream of the vortex pairing). The imaginary part of k_0 is more dependent on the component chosen; however as noted earlier, the solution is not very sensitive to the value of the imaginary part.

The location where the model was applied, $x_1 = x_m$, was chosen to be as upstream as possible (but downstream of the vortex pairing) consistent with the requirement that the real part of k_0 become as independent of x_1 as possible. For the case shown in figure 12, the values of x_m used were $35R_0$ for the fundamental frequency, $40R_0$ for the first subharmonic frequency, and $45R_0$ for the $\frac{3}{2}f_0$ and $2f_0$ frequencies.

While the axial extent of the sources is large, the radial extent is small; the source terms are only significant where the vorticity is non-zero, say $r < 3R_0$. This observation was anticipated by the acoustic theories of Powell (1964), Howe (1975), and Möhring (1978) who showed that the acoustic source terms could be expressed in terms of the vorticity.

4.2. *Solution method*

Our solution method borrows ideas from Ffowcs Williams & Kempton (1978), Mankbadi & Liu (1984) and Mankbadi (1990). Mankbadi & Liu (1984) and Mankbadi (1990) solved Lighthill's equation to determine the sound generated by rapidly growing and decaying instability waves. Their solution method made no assumption about acoustical compactness in the axial direction and assumed slight acoustical non-compactness in the radial direction. Ffowcs Williams & Kempton (1978) considered the sound generated by a non-decaying, convecting source. They assumed that the source was acoustically compact. We will consider the source to be non-compact. See also the recent discussion of the numerical solution of Lighthill's equation in Bastin, Lafon & Candel (1997).

4.2.1. *Solution in the active region*

Our starting point is the temporal Fourier transform of Lighthill's equation:

$$\nabla^2_{(y)}\hat{\rho} + \left(\frac{\omega}{c_\infty}\right)^2 \hat{\rho} = -\frac{1}{c_\infty^2}\frac{\partial^2}{\partial y_i\,\partial y_j}\hat{T}_{ij}(\boldsymbol{y}), \tag{4.5}$$

which has a solution in terms of its Green's function,

$$\hat{\rho}(\boldsymbol{x}) = \frac{1}{c_\infty^2}\int_V \frac{\partial^2 \hat{T}_{ij}(\boldsymbol{y})}{\partial y_i\,\partial y_j}\frac{\mathrm{e}^{\mathrm{i}\omega R/c_\infty}}{4\pi R}\,\mathrm{d}\boldsymbol{y} \tag{4.6}$$

where $\boldsymbol{R} = \boldsymbol{x} - \boldsymbol{y}$, $R = |\boldsymbol{R}|$ and V is the volume of space over which the sources are non-zero. Using integration by parts and the divergence theorem, the derivatives are transferred from the source, $\hat{T}_{ij}$, to the Green's function

$$\hat{\rho}(\boldsymbol{x}) = \frac{1}{c_\infty^2}\int_V \hat{T}_{ij}(\boldsymbol{y})\frac{\partial^2}{\partial x_i\,\partial x_j}\left(\frac{\mathrm{e}^{\mathrm{i}\omega R/c_\infty}}{4\pi R}\right)\mathrm{d}\boldsymbol{y}, \tag{4.7}$$

where we have used the identity $\partial R/\partial y_i = -\partial R/\partial x_i$. Evaluating the derivatives yields

$$\hat{\rho}(\boldsymbol{x}) = -\frac{\omega^2}{c_\infty^4}\int_V \frac{R_iR_j}{R^2}\hat{T}_{ij}\frac{\mathrm{e}^{\mathrm{i}\omega R/c_\infty}}{4\pi R}\mathrm{d}\boldsymbol{y} + O\left(\frac{\lambda}{2\pi R}\right) \tag{4.8}$$

where our notation means that the neglected terms are a factor of $O\left(\lambda/(2\pi R)\right)$ times smaller than the retained terms and where $\lambda = 2\pi c_\infty/\omega$ is the wavelength of the sound waves. In cylindrical coordinates, this is

$$\hat{\rho}(\boldsymbol{x}) = -\frac{\omega^2}{c_\infty^4}\int_{-\infty}^{\infty}\int_0^{\infty}\int_0^{2\pi}\sigma R_iR_j\hat{T}_{ij}\frac{\mathrm{e}^{\mathrm{i}\omega R/c_\infty}}{4\pi R^3}\mathrm{d}\phi\,\mathrm{d}\sigma\,\mathrm{d}y_1 \tag{4.9}$$

where x_1 and r are the cylindrical coordinate components of $\boldsymbol{x}$ and y_1, σ, and ϕ are the components of $\boldsymbol{y}$, and where

$$R^2 = (x_1 - y_1)^2 + r^2 + \sigma^2 - 2r\sigma\cos(\phi). \tag{4.10}$$

Our next step is to transform the source tensor, $\hat{T}_{ij}$, from Cartesian to cylindrical coordinates by recognizing that $R_iR_j\rho u_iu_j = \rho(\boldsymbol{R}\cdot\boldsymbol{u})^2$ which leads to

$$\frac{R_iR_j}{\xi^2}\hat{T}_{ij}(\boldsymbol{y}) = \sum_{j=0}^{2}A_j(\boldsymbol{x},\boldsymbol{y})\cos^j(\phi) + O\left(\frac{\sigma}{R}\right), \tag{4.11}$$

where

$$\left.\begin{aligned} A_0 &= \cos^2(\theta)\,\widehat{\rho uu} + (\hat{p} - c_\infty^2\hat{\rho}),\\ A_1 &= 2\cos(\theta)\sin(\theta)\,\widehat{\rho uv_r},\\ A_2 &= \sin^2(\theta)\,\widehat{\rho v_rv_r}, \end{aligned}\right\} \tag{4.12}$$

and where $\xi = R_1^2 + r^2$, $\cos(\theta) = R_1/\xi$, and $\sin(\theta) = r/\xi$. Recall that $R_1 = x_1 - y_1$. Thus, the solution becomes

$$\hat{\rho}(\boldsymbol{x}) = -\frac{\omega^2}{c_\infty^4}\int_{-\infty}^{\infty}\int_0^{\infty}\sigma\sum_{j=0}^{2}A_j(\boldsymbol{x},\boldsymbol{y})\,\hat{g}_j(\boldsymbol{x},\boldsymbol{y})\,\mathrm{d}\sigma\,\mathrm{d}y_1, \tag{4.13}$$

where the ‘Green’s function’, $\hat{g}_j$, is given by

$$\hat{g}_j(\boldsymbol{x},\boldsymbol{y}) = \xi^2\int_0^{2\pi}\cos^j(\phi)\frac{\mathrm{e}^{\mathrm{i}\omega R/c_\infty}}{4\pi R^3}\mathrm{d}\phi. \tag{4.14}$$

The trigonometric functions of θ in A_j should be viewed as part of the Green’s function. For low frequencies, it is possible to develop a series expansion for $\hat{g}_j$; however, this expansion is not convergent at higher frequencies. Thus we evaluated $\hat{g}_j$ using numerical integration of equation (4.14) via the trapezoidal rule using between 8 and 32 points depending on the frequency.

Since the solution to Lighthill’s equation, (4.13), is a convolution integral, it is computationally expensive to evaluate. There are two ways to proceed. First, we could expand equation (4.13) in a multipole expansion (Goldstein 1976, § 1.5.2) about $y_1 = \sigma = 0$. We explored this approach; however numerical difficulties associated with computing the higher order moment integrals (that arise for acoustically non-compact sources) prevented us from obtaining accurate far-field predictions. In addition, a multipole approach requires the source location as input.

The second approach, and the approach used for the results presented herein, is to approximate equation (4.13) by subdividing the integration domain into rectangular regions of size $\Delta y_1 \times \Delta\sigma$. In each small region, the Green’s function and functions of

θ in A_j are evaluated by assuming that $\boldsymbol{y}$ is fixed at the centroid of the region. The results from each subdivision are then summed to obtain the far-field prediction. The size of the subdivisions is chosen to ensure that the regions are acoustically compact as measured by the axial and radial Helmholtz numbers, $\omega \Delta y_1/c_\infty$ and $\omega \Delta \sigma/c_\infty$. Our value for the Helmholtz number is discussed at the end of the next section.

The (infinite) upper limit on the radial integral is taken as $3R_0$ and the limits on the axial integral are taken to include only the active region, i.e. $0 \leqslant y_1 \leqslant x_m$. The axial integral in the passive region, $x_m < y_1 \leqslant \infty$, is the topic of the next section.

4.2.2. *Solution in the passive region*

In the passive region, we substitute (4.3) into (4.9) to find

$$\hat{\rho}(\boldsymbol{x}) = -\frac{\omega^2}{c_\infty^4}\int_0^\infty \sigma \hat{T}_{ij} \int_0^{2\pi}\int_0^\infty \mathrm{e}^{\mathrm{i}k_0 y_1}\left[\frac{R_i R_j\,\mathrm{e}^{\mathrm{i}\omega R/c_\infty}}{4\pi R^3}\right]\mathrm{d}y_1\,\mathrm{d}\phi\,\mathrm{d}\sigma, \tag{4.15}$$

where $\hat{T}_{ij}$ is a function only of σ and where, without loss of generality, x_m is taken as $x_m = 0$. Expanding the bracketed term as a Taylor series about $y_1 = 0$ and neglecting terms that are small in the far field:

$$\hat{\rho}(\boldsymbol{x}) = -\frac{\omega^2}{c_\infty^4}\int_0^\infty \sigma \hat{T}_{ij}\int_0^{2\pi}\sum_{n=0}^{\infty}\left[\left(\frac{\omega x_1}{\eta c_\infty}\right)^n \int_0^\infty \frac{(-\mathrm{i}y_1)^n}{n!}\mathrm{e}^{\mathrm{i}k_0 y_1}\mathrm{d}y_1\right] \times\frac{\eta_i\eta_j\,\mathrm{e}^{\mathrm{i}\omega\eta/c_\infty}}{4\pi\eta^3}\mathrm{d}\phi\,\mathrm{d}\sigma + O\left(\frac{\lambda}{2\pi\eta}\right) \tag{4.16}$$

where η is R evaluated at $y_1 = 0$. The y_1 integral is Euler's integral (see Abramowitz & Stegun 1964, equation 6.1.1) and can be evaluated analytically to yield

$$\hat{\rho}(\boldsymbol{x}) = -\frac{\omega^2}{c_\infty^4}\int_0^\infty \sigma \hat{T}_{ij}\int_0^{2\pi}\frac{\mathrm{i}}{k_0}\sum_{n=0}^{\infty}\left(M_k x_1/\eta\right)^n \frac{\eta_i\eta_j\,\mathrm{e}^{\mathrm{i}\omega\eta/c_\infty}}{4\pi\eta^3}\mathrm{d}\phi\,\mathrm{d}\sigma \tag{4.17}$$

where

$$M_k = \frac{\omega}{c_\infty k_0}\ . \tag{4.18}$$

The summation can be expressed in closed form:

$$\hat{\rho}(\boldsymbol{x}) = -\frac{\omega^2}{c_\infty^4}\int_0^\infty \sigma \hat{T}_{ij}\int_0^{2\pi}\frac{\mathrm{i}/k_0}{1 - M_k x_1/\eta}\frac{\eta_i\eta_j\,\mathrm{e}^{\mathrm{i}\omega\eta/c_\infty}}{4\pi\eta^3}\mathrm{d}\phi\,\mathrm{d}\sigma \tag{4.19}$$

assuming that $|M_k\cos(\theta)| < 1$. Finally, the source tensor is converted from Cartesian to cylindrical coordinates:

$$\hat{\rho}(\boldsymbol{x}) = -\frac{\omega^2}{c_\infty^4}\sum_{j=0}^{2}\int_0^\infty \sigma A_j \tilde{g}_j(\boldsymbol{x},\boldsymbol{y})\,\mathrm{d}\sigma + O\left(\frac{\sigma}{\eta}\right) \tag{4.20}$$

where

$$\tilde{g}_j(\boldsymbol{x},\boldsymbol{y}) = \frac{\mathrm{i}\xi^2}{k_0}\int_0^{2\pi}\frac{\mathrm{e}^{\mathrm{i}\omega\eta/c_\infty}}{4\pi\eta^3(1 - M_k x_1/\eta)}\mathrm{d}\phi. \tag{4.21}$$

In a manner similar to the discussion after equation (4.14), equation (4.20) is solved by subdividing the radial domain into small, acoustically compact regions of size $\Delta\sigma$; the upper limit of the radial integral was taken as $3R_0$. In both the active and passive regions, the radial Helmholtz number, $\omega\Delta r/c_\infty$, was taken as 0.1. The axial

Helmholtz number, $\omega \Delta y_1/c_\infty$, needed only in the active region, was taken as 0.05; the lower value of the axial Helmholtz number was required in order to match the exact axial integration performed in the passive region. The contributions from all the small regions in both the active and passive region are combined to determine the complete far-field prediction.

In order to compare the Lighthill predictions to the direct computations, the far-field density fluctuations are converted to dilatation fluctuations via

$$\hat{\Theta} = \frac{\mathrm{i}\omega}{\rho_\infty}\hat{\rho}. \tag{4.22}$$

4.3. *Comparison to DNS*

Predictions obtained using Lighthill's equation are shown in figure 13 for the thick shear layer jets at various frequencies. With the exception of the $2f_0$ frequency, the predictions are in good agreement with the directly computed data. It is interesting to note that although Lighthill's equation qualitatively predicts most of the observed angles of extinction, there are some minor quantitative differences. For instance at the fundamental frequency of the $M_j = 0.4$ jet, Lighthill's equation predicts the angle of extinction at 68° compared to the actual location at 72°. Since the angles of extinction are quiet regions of the far field that result from destructive interference, it not surprising that this is a difficult feature of the far field for the prediction to capture accurately.

Note that these predictions were obtained for large x ($x = 70R_0$) in order to ensure the validity of various approximations made in § 4.2. For example, the worst case for the approximation in (4.8) occurs for the first subharmonic frequency of the $M_j = 0.4$ jet where we estimate that the error term, $\lambda/(2\pi x)$, yields a 5% error. Although Lighthill's equation can be solved for any value of x and θ, the directly computed data are only available for a finite region of space. Thus, as a result of the large value of x, figure 13 does not include shallow angles. We also made comparisons (not shown) of Lighthill's equation at $x = 40R_0$. These comparisons verified that predictions at shallower angles to the jet axis are also in good agreement with the computational data.

Lighthill predictions for the thin shear layer, $M_j = 0.8$ jet are shown in figure 14. The results are similar to the thick shear layer jets. In particular, good agreement is seen at lower frequencies; however the accuracy is not as good for the higher frequencies. Recall from § 4.1 that the model used for the extensive source region is not as accurate a description of the source terms at higher frequency. By examining the sensitivity of the Lighthill predictions to x_m, we were able to show that the discrepancies at higher frequencies (for all the jets) are due to the model.

Despite its relatively poorer performance at high frequency, it is essential to include a model for the passive region of the source. Predictions obtained by truncating the source data at $x_1 = X_p$ typically over-predicted the far-field sound by an order of magnitude, see figure 15 for an example. Mitchell *et al.* (1995*b*) demonstrate that it is essential to include the effects of axial source non-compactness when calculating the Lighthill predictions.

In summary, predictions obtained using Lighthill's equation are in good agreement with the directly computed results and the inclusion of a model for the extensive spatial distribution of the Lighthill stress tensor is essential. Most of the discrepancies are at higher frequencies and can be attributed to the fact that the accuracy of the

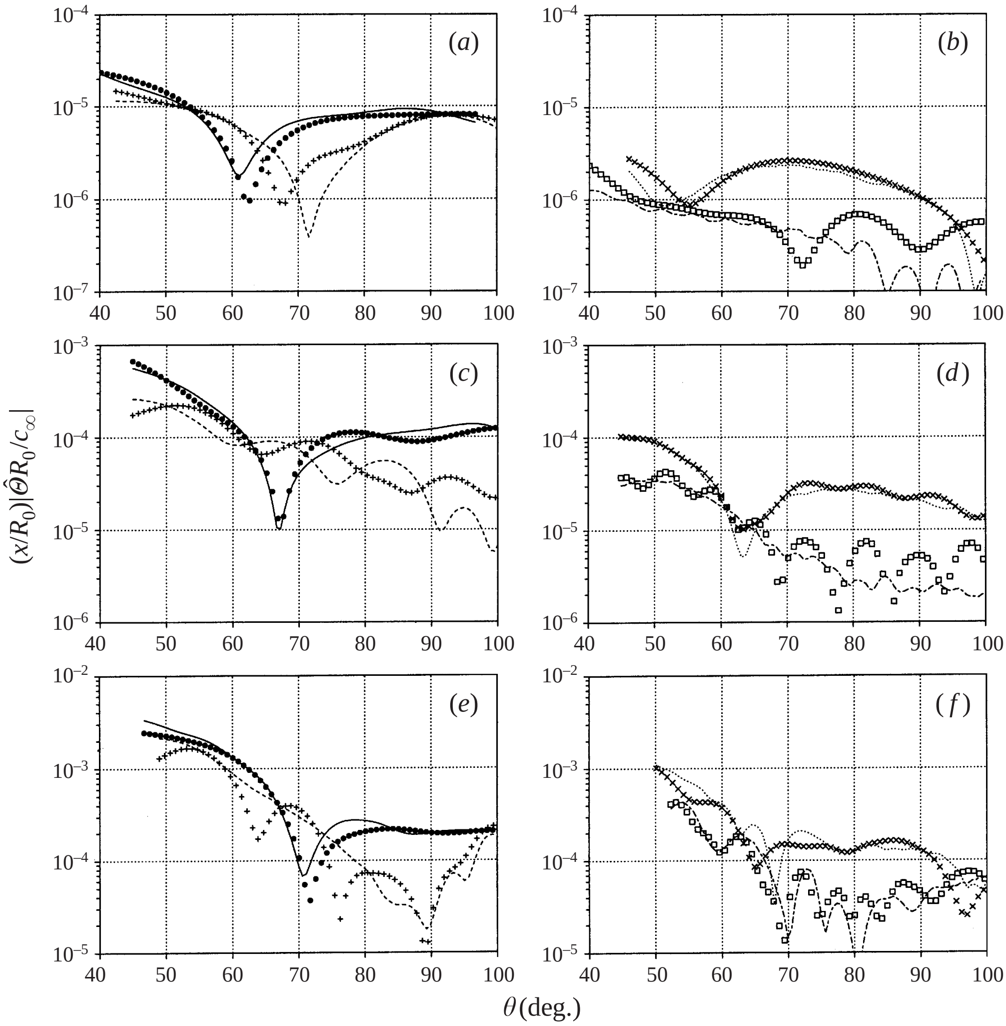

FIGURE 13. Comparison of the directly computed sound (lines) to predictions obtained using Lighthill's equation (symbols). The plots are for the jets: (a,b) $M_j = 0.4$; (c,d) $M_j = 0.8$; and (e,f) $M_j = 1.2$. Shown is the magnitude of the Fourier transform of the dilatation at a distance of $x = 70R_0$ from the apparent source location, x_s. In (a,c,e) the curves are for $\frac{1}{2}f_0$ (———, ●); and f_0(– – – –, +). In plots (b,d,f) the curves are for $\frac{3}{2}f_0$ (········, ×); and $2f_0$ (— — —, □).

model introduced to handle the extensive spatial distribution of the source terms decreases with increasing frequency.

5. Kirchhoff surface method

5.1. *Formulation*

The Kirchhoff surface method of predicting sound is based on an analytical formula that relates the sound to integrals over a closed surface that surrounds all acoustic sources. Kirchhoff's formula, which forms the basis of the technique, has been known for some time, see Kirchhoff (1883). Lyrintzis (1994) reviews recent aeroacoustic applications, see also Brentner & Farassat (1997).

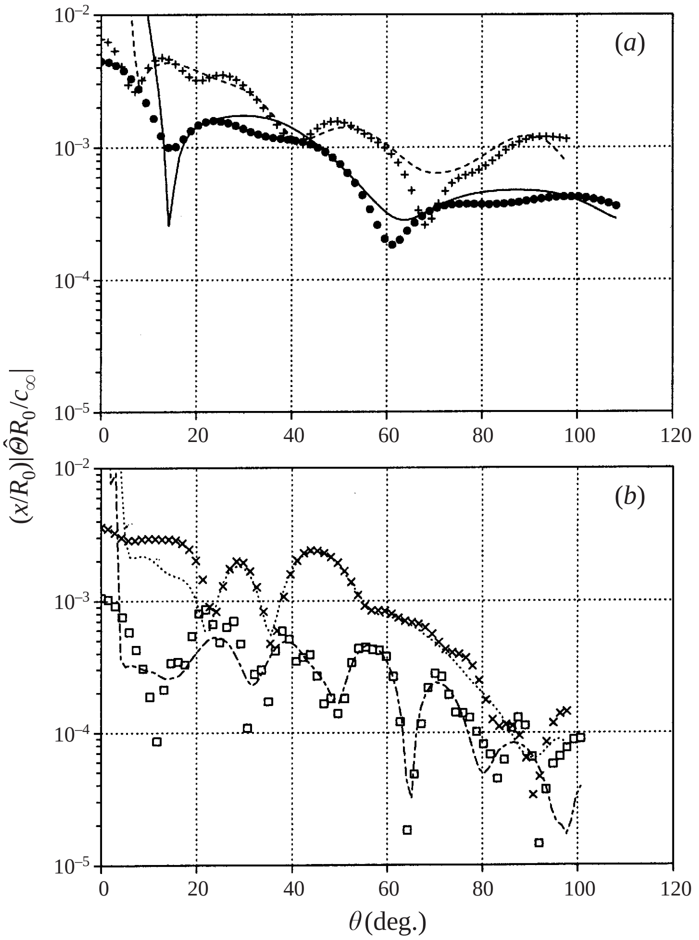

FIGURE 14. Comparison of the directly computed sound (lines) from the thin shear layer, $M_j = 0.8$ jet to predictions obtained using Lighthill's equation (symbols) at various frequencies. Shown is the magnitude of the Fourier transform of the dilatation at a distance of $x = 40R_0$ from the apparent source location, x_s. In plot (*a*), the curves are for: $\frac{1}{4}f_0$ (———, ●); and $\frac{1}{2}f_0$ (– – – –, +); In plot (*b*), the curves are for: f_0 (········, ×); and $\frac{3}{2}f_0$ (— — —).

Our starting point is the Kirchhoff–Helmholtz equation which relates the temporal Fourier transform of an acoustic variable, say $\hat{\varphi}$, to surface integrals of $\hat{\varphi}$ and its derivative normal to the surface:

$$\hat{\varphi}(\boldsymbol{x};\omega) = \int_S \left[\frac{\partial \hat{\varphi}(\boldsymbol{y})}{\partial \boldsymbol{n}(\boldsymbol{y})} \hat{G}(\boldsymbol{x},\boldsymbol{y}) - \hat{\varphi} \frac{\partial \hat{G}}{\partial \boldsymbol{n}} \right] \mathrm{d}S(\boldsymbol{y}), \tag{5.1}$$

where $\boldsymbol{n}$ is the outward pointing normal on the surface S (the 'Kirchhoff surface'), and $\hat{G}$ is the Green's function of the Helmholtz or reduced wave equation. The Kirchhoff–Helmholtz equation can be developed using vector calculus (Pierce 1989, §4–6) or generalized functions, see Farassat (1977) and Farassat & Myers (1988). If $\boldsymbol{x}$ is inside S, then (5.1) evaluates to $\hat{\varphi} = 0$. The form of the Kirchhoff–Helmholtz equation given in (5.1) is appropriate for a stationary surface. If the mean velocity is non-zero in the far field, then a Kirchhoff–Helmholtz equation for a moving surface should be used, see Ffowcs Williams & Hawkings (1969), Farassat & Myers (1988) and Myers

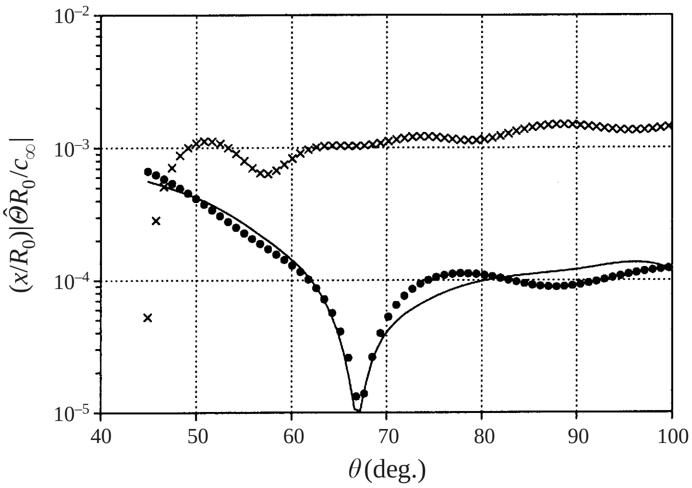

FIGURE 15. Comparison of predictions obtained from the solution of Lighthill's equation with and without a model for the slow decay of the source terms. The predictions are for first subharmonic frequency of the $M_j = 0.8$ jet at a distance of $x = 70R_0$ from the apparent source location, x_s. The curves are for: DNS data (———); Lighthill prediction including model for passive region (●); and Lighthill prediction with no model for the passive region (×).

& Hausmann (1990) for details. For a jet, the logical choice of S is an open-ended cylinder of radius R_s. For such a surface when $\hat{\varphi}(\boldsymbol{y})$ is independent of the azimuthal direction (as for the present case of axisymmetric jets), the Kirchhoff–Helmholtz equation reduces to

$$\hat{\varphi}(\overbrace{x_1, r}^{x}; \omega) = R_s \int_{-\infty}^{\infty} \left[\frac{\partial \hat{\varphi}(\overbrace{y_1, R_s}^{y})}{\partial r} \hat{g} - \hat{\varphi} \frac{\partial \hat{g}}{\partial r} \right] \mathrm{d}y_1, \tag{5.2}$$

where $\hat{g}(x_1, r, y_1, R_s)$ is computed via

$$\hat{g}(x_1, r, y_1, R_s) = \int_0^{2\pi} -\frac{\mathrm{e}^{\mathrm{i}\omega R/c_\infty}}{4\pi R} \mathrm{d}\phi, \tag{5.3}$$

and where, $R^2 = (x_1 - y_1)^2 + r^2 + R_s^2 - 2R_s r \cos(\phi)$. Note that it is possible to show that

$$\hat{g}(x_1, r, y_1, R_s) \approx -\mathrm{J}_0\left(\frac{\omega R_s}{c_\infty}\frac{r}{\xi}\right)\frac{\mathrm{e}^{\mathrm{i}\omega\xi/c_\infty}}{2\xi} \tag{5.4}$$

where $\xi^2 = (x_1 - y_1)^2 + r^2$ and where $\mathrm{J}_0(x)$ is the zeroth-order Bessel function of the first kind provided that $x \gg y$. However, since we did not want to restrict our results to $x \gg y$, we evaluated $\hat{g}$ using numerical evaluation of (5.3).

The use of a Kirchhoff surface as a tool to calculate the far-field sound proceeds by specifying the values of $\hat{\varphi}$ on the surface S using computational data. Then the integral in (5.2) is evaluated using numerical quadrature to find $\hat{\varphi}$ outside the surface. The infinite limits on the integral are replaced with the range $0 \leqslant y_1 \leqslant X_p$.

The errors introduced by truncating the integral have been analysed recently by Freund, Lele & Moin (1997) who developed a geometric criterion that determines when the truncation of the Kirchhoff surface will not lead to significant error. They suggest that if a line between the far-field observer and the apparent sound source

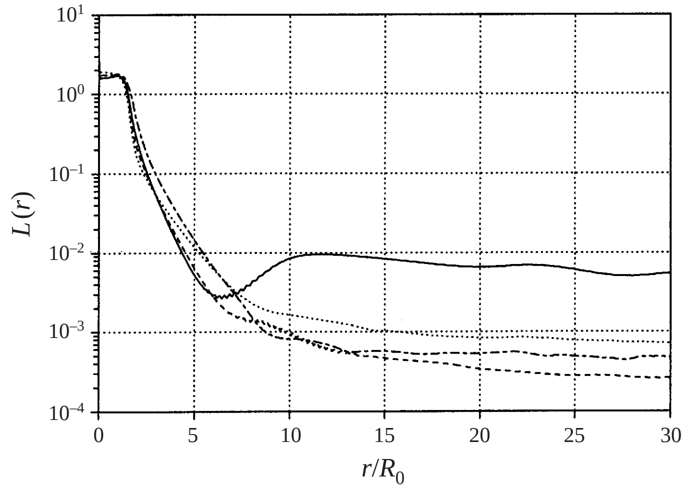

FIGURE 16. The difference between the time rate of change of the flow variables as computed using the Navier–Stokes equations and the linearized Euler equations: ———, $M_j = 0.4$; ----, $M_j = 0.8$; ········, $M_j = 1.2$; and — — —, thin shear layer, $M_j = 0.8$.

intersects the Kirchhoff surface in the region included in the integration, $0 \leqslant x_1 \leqslant X_p$, then errors from truncating the integral will be small. If, however, the vector intersects the Kirchhoff surface in a region where the data are not included in the integration, then errors will dominate the solution. In order to reduce the volume of the far field where errors would be expected to dominate, the radius of the Kirchhoff surface should be small and the length of the surface should be as large as possible.

Three issues remain:

(i) Is the mean velocity in the far field small enough to justify the use of the Kirchhoff–Helmholtz formula? The mean velocity in the far field is due to entrainment and we found that the Mach number of the entrainment flow is less than 0.005 for $r > 5R_0$. Thus the mean flow may be neglected and use of the Kirchhoff–Helmholtz equation is justified.

(ii) How should the location of the Kirchhoff surface, R_s, be chosen? The value of R_s must be sufficiently large that the Navier–Stokes equations reduce to the linearized Euler equations at S but, as just noted above, should be small to minimize errors associated with truncating the infinite integrals. In § 5.2 we will choose R_s by directly comparing the Navier–Stokes and linearized Euler equations.

(iii) What acoustic variables should be used for $\hat{\varphi}$? Previous applications of the Kirchhoff surface method have used the pressure as the acoustic variable in (5.2), see for instance Lyrintzis & Mankbadi (1995). However, we use the fluid dilatation, $\Theta = \nabla \cdot \boldsymbol{u}$. Note that dilatation is directly related to the far-field pressure via

$$\Theta = -\frac{1}{\rho_\infty c_\infty^2}\frac{\partial p}{\partial t}. \tag{5.5}$$

5.2. *Comparison to DNS*

Before comparing the far-field sound predicted using a Kirchhoff surface to the directly computed results, we must choose the radius of the Kirchhoff surface. First, we compare the time rate of change of the flow variables computed using the Navier–

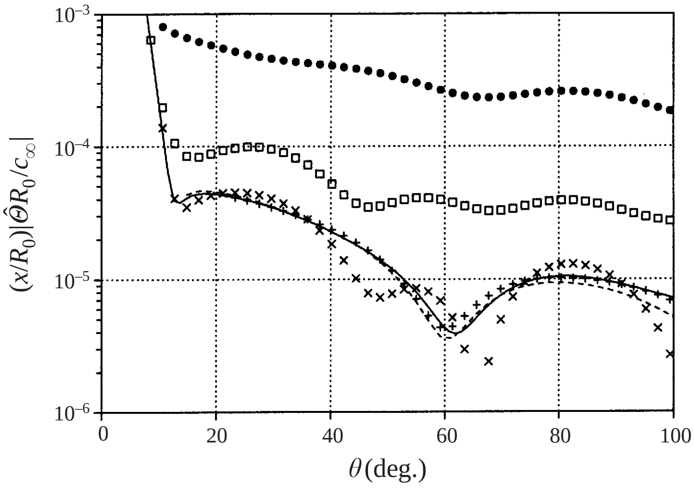

FIGURE 17. Comparison of the directly computed sound to predictions obtained from Kirchhoff surfaces located at different distances from the centreline for the $M_j = 0.4$ jet at the first subharmonic frequency. Shown is the magnitude of the Fourier transform of the dilatation at a distance of $x = 40R_0$ from the apparent source locations, x_s: ———, DNS; Kirchhoff surface at ●, $R_s = 3R_0$; □, $R_s = 5R_0$; ----, $R_s = 7R_0$; ×, ----, $R_s = 10R_0$; and +, $R_s = 15R_0$.

Stokes and linearized Euler equations, i.e. we consider the quantity L defined via

$$L^2(r) = \int_0^{X_p} |\boldsymbol{v}_{\mathrm{NS}} - \boldsymbol{v}_{\mathrm{Euler}}|^2 \, \mathrm{d}x_1 \bigg/ \int_0^{X_p} |\boldsymbol{v}_{\mathrm{NS}}|^2 \, \mathrm{d}x_1 \tag{5.6}$$

where $\boldsymbol{v} = (\dot{u}/c_\infty, \dot{v}_r/c_\infty, \dot{\rho}/\rho_\infty)^T$ and subscripts denote the Navier–Stokes and linearized Euler equations. Figure 16 shows L for the different jets. It is seen that the Navier–Stokes equations rapidly approach the linearized Euler equations until $r \approx 10R_0$. It is believed that the slow decay for $r > 10R_0$ is caused by the slow decay of the entrainment flow, i.e. the actual mean flow slowly approaches the zero mean flow assumed for the linearized Euler equations. Comparisons of the Euler and linearized Euler equations demonstrated that the slow decay for $r > 10R_0$ is not due to the viscous terms.

In order to determine if the surface can be located closer than $10R_0$, we compare predictions using R_s in the range $3R_0 \leqslant R_s \leqslant 15R_0$ to the directly computed sound. This is shown in figure 17 for the subharmonic frequency of the $M_j = 0.4$ jet. The comparison shows that $R_s = 10R_0$ is an appropriate location for the Kirchhoff surface. Comparisons at other Mach numbers and frequencies reached the same conclusion. At higher frequencies, we observed that the surface may be located closer to the centreline, for instance the surface may be located as close as $R_s = 5R_0$ for the $2f_0$ frequency of the $M_j = 0.4$ jet.

Predictions obtained using the Kirchhoff surface method are compared to the directly computed data in figures 18 and 19. The predictions are in excellent agreement with the directly computed results.

In the calculations discussed in this study, the computational domain extends several acoustic wavelengths into the far field and contamination of the flow at the Kirchhoff surface by the numerical boundary conditions is not significant. If the computational boundary was located in the same region of the flow as the Kirchhoff

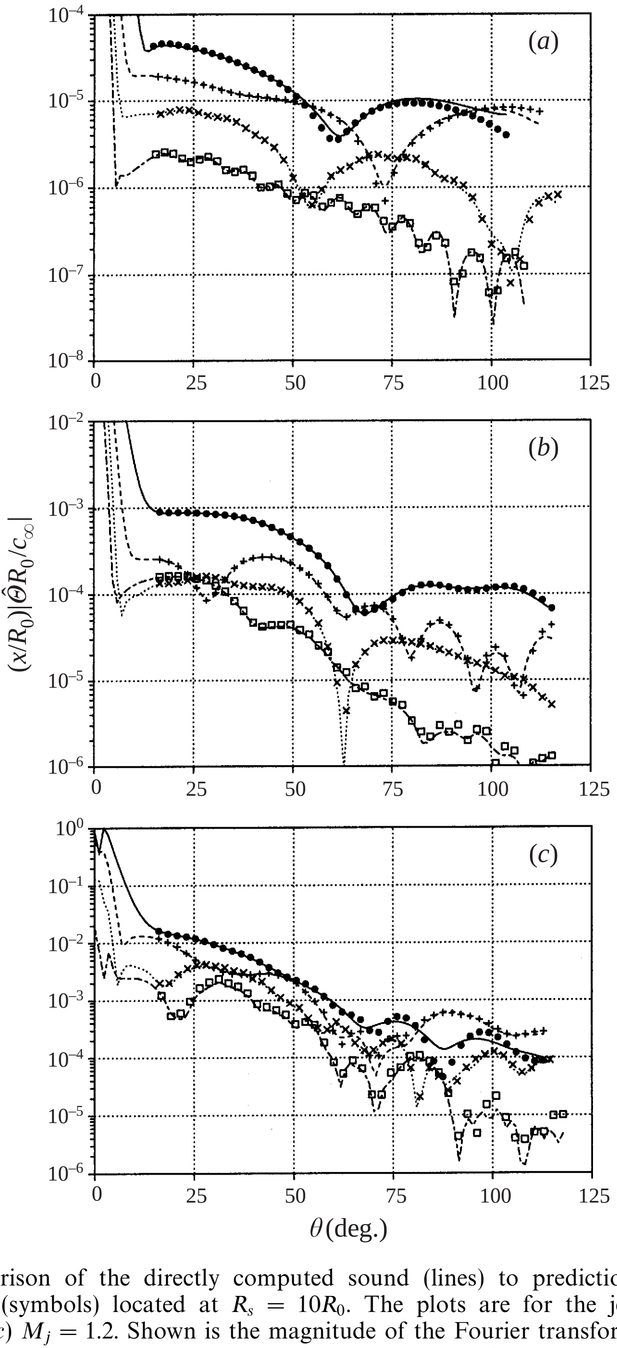

FIGURE 18. Comparison of the directly computed sound (lines) to predictions obtained using Kirchhoff surfaces (symbols) located at $R_s = 10R_0$. The plots are for the jets: (*a*) $M_j = 0.4$; (*b*) $M_j = 0.8$; and (*c*) $M_j = 1.2$. Shown is the magnitude of the Fourier transform of the dilatation at a distance of $x = 70R_0$ from the apparent source location, x_s: $\frac{1}{2}f_0$ (———, ●); f_0 (- - - -, +); $\frac{3}{2}f_0$ (········, ×); and $2f_0$ (— — —, □).

surface, as might well occur in practice, there is the possibility that the data on the Kirchhoff surface will be affected by the boundary conditions. This is an important issue that warrants further investigation to assess the proper location of the Kirchhoff surface and top boundary.

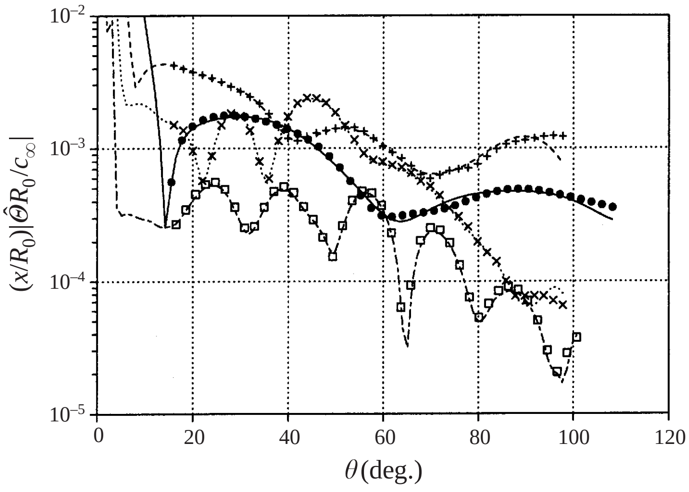

FIGURE 19. As figure 18 but for the thin shear layer $M_j = 0.8$ jet. Shown is the magnitude of the Fourier transform of the dilatation at a distance of $x = 40R_0$ from the apparent source location, x_s. The curves are for: $\frac{1}{4}f_0$ (——, ●); $\frac{1}{2}f_0$ (– – – –, +); f_0 (·······, ×); and $\frac{3}{2}f_0$ (— – —, □).

6. Conclusions

The sound generated by vortex pairing in axisymmetric jets has been directly computed by numerical solution of the compressible Navier–Stokes equations on a computational domain that includes both the near and far fields. Direct computations of four jets were presented. The far-field sound from the lowest Mach number jet ($M_j = 0.4$) resembles the sound from axisymmetric point quadrupoles similar to the experiments of Bridges & Hussain (1992) while the sound from the highest speed jet ($M_j = 1.2$) is superdirective in the sense of Crighton & Huerre (1990).

The directly computed far-field sound was compared to predictions obtained by solving Lighthill's equation where the Lighthill stress tensor was evaluated using the simulation data. The large spatial extent of the Lighthill stress tensor necessitated the introduction of a model to describe its behaviour in the region downstream of the outflow boundary. Overall, the Lighthill predictions are in good agreement with the directly computed data and we demonstrated that the inclusion of a model for the downstream behaviour of the Lighthill stress tensor is essential. We caution that it is imperative not to assume acoustical compactness when solving Lighthill's equation. As partial proof of this statement, we recall that the phenomenon of superdirectivity (observed in the $M_j = 1.2$ jet) is directly the result of acoustical non-compactness and cannot be properly predicted unless acoustical non-compactness is accounted for in the solution of Lighthill's equation.

It must be noted that the smallest acoustic wavelength presented in this paper was $2.4R_0$ (corresponding to the $2f_0$ frequency of the $M_j = 1.2$ jet). As such, the acoustic waves in this study propagated a distance through the non-zero mean flow that was short compared to the acoustic wavelength and thus modification of the sound (level and/or directivity) by the mean flow was not anticipated. For higher frequency sound waves (and thus shorter wavelengths), modification of the sound waves by the mean flow, e.g. refraction and scattering, is anticipated and it is likely the predictions from Lighthill's equation would not be as good. In such situations, the use of higher order wave equations, e.g. Lilley's equation (Goldstein 1976, chapter 6; Colonius *et al.* 1997), may be necessary.

The directly computed data were also compared to predictions obtained using the Kirchhoff surface method. We presented a technique based on comparison of the Navier–Stokes and linearized Euler equations to locate the Kirchhoff surface. The Kirchhoff surface predictions are in excellent agreement with directly computed data.

This work has been sponsored by the Office of Naval Research, grant N00014-92-J-1626, and computer time has been provided by the NASA Ames Research Center through the Center for Turbulence Research and by the Numerical Aerodynamic Simulation (NAS) Program. The first author acknowledges financial support from the Franklin P. and Caroline M. Johnson fellowship.

REFERENCES

Abramowitz, M. & Stegun, I. 1964 *Handbook of Mathematical Functions.* Dover.

Bastin, F., Lafon, P. & Candel, S. 1997 Computation of jet mixing noise due to coherent structures: the plane jet case. *J. Fluid Mech.* **335**, 261–304.

Brentner, K. S. & Farassat, F. 1997 An analytical comparison of the acoustic analogy and Kirchhoff formulation for moving surfaces *Proc. 53rd AHS Forum, Virginia Beach, VA, April 29 – May 1*, p. 687.

Bridges, J. & Hussain, F. 1992 Direct evaluation of aeroacoustic theory in a jet. *J. Fluid Mech.* **240**, 469–501.

Colonius, T., Lele, S. K. & Moin, P. 1993 Boundary conditions for direct computation of aerodynamic sound generation. *AIAA J.* **31**, 1574–1582.

Colonius, T., Lele, S. K. & Moin, P. 1994 The scattering of sound waves by a vortex – numerical simulations and analytical solutions. *J. Fluid Mech.* **260**, 271–298.

Colonius, T., Lele, S. K. & Moin, P. 1995*a* The sound generated by a two-dimensional shear layer: A comparison of direct computations and acoustic analogies. Presented at the *First Joint CEAS/AIAA Aeroacoustics Conference, Munich Germany, June 12–15, 1995.*

Colonius, T., Lele, S. K. & Moin, P. 1997 Sound generation in a mixing layer. *J. Fluid Mech.* **330**, 375–409.

Colonius, T., Moin, P. & Lele, S. K. 1995*b* Direct computation of aerodynamic sound. *Rep.* TF-65. Department of Mechanical Engineering, Stanford University.

Crighton, D. G. 1972 The excess noise field of subsonic jets. *J. Fluid Mech.* **56**, 683–694.

Crighton, D. G. 1993 Computational aeroacoustics for low Mach number flows. *In Computational Aeroacoustics* (ed. H. Hardin & M. Y. Hussaini), pp. 51–68. Springer.

Crighton, D. G. & Huerre, P. 1990 Shear-layer pressure fluctuations and superdirective acoustic sources. *J. Fluid Mech.* **220**, 355–368.

Crow, S. C. 1970 Aerodynamic sound emission as a singular perturbation problem. *Stud. Appl. Maths.* **49**, 21–44.

Farassat, F. 1977 Discontinuities in aerodynamics and aeroacoustics: The concept and applications of generalized derivatives. *J. Sound Vib.* **55**, 165–193.

Farassat, F. & Myers, M. K. 1988 Extension of Kirchhoff's formula to radiation from moving surfaces. *J. Sound Vib.* **123**, 451–460.

Ffowcs Williams, J. E. & Hawkings, D. L. 1969 Sound generation by turbulence and surfaces in arbitrary motion. *Phil. Trans. R. Soc. Lond.* A **264**, 321–342.

Ffowcs Williams, J. E. & Kempton, J. 1978 The noise from the large-scale structure of a jet. *J. Fluid Mech.* **84**, 673–694.

Freund, J. B., Lele, S. K. & Moin, P. 1996 Calculation of the radiated sound field using an open Kirchhoff surface. *AIAA J.* **34**, 909–916.

Giles, M. B. 1990 Non-reflecting boundary conditions for Euler equation calculations. *AIAA J.* **28**, 2050–2058.

Goldstein, M. E. 1976 *Aeroacoustics.* McGraw Hill.

Ho, C.-M. & Huang, L.-S. 1982 Subharmonics and vortex merging in mixing layers. *J. Fluid Mech.* **119**, 443–473.

Howe, M. S. 1975 Contributions to the theory of aerodynamic sound, with application to excess noise and the theory of the flute. *J. Fluid Mech.* **71**, 625–673.

Huerre, P. & Crighton, D. 1983 Sound generation by instability waves in a low Mach number jet. *AIAA Paper* 83–0661.

Kibens, V. 1979 Discrete noise spectrum generated by an acoustically excited jet. *AIAA J.* **18**, 434–441.

Kirchhoff, G. R. 1883 Towards a theory of light rays. *Ann. Phys. Chem.* **18**, 663–695.

Laufer, J. & Yen, T.-C. 1983 Noise generation by a low-Mach-number jet. *J. Fluid Mech.* **134**, 1–31.

Laufer, J. & Zhang, J. X. 1983 Unsteady aspects of a low Mach number jet. *Phys. Fluids* **26**, 1740–1750.

Lele, S. K. 1992 Compact finite difference schemes with spectral-like resolution. *J. Comput. Phys.* **103**, 16–42.

Lighthill, J. 1952 On sound generated aerodynamically I. General theory. *Proc. R. Soc. Lond.* A **211**, 564–587.

Lyrintzis, A. 1994 A review of the uses of Kirchhoff's method in computational aeroacoustics. *Trans. ASME: J. Fluids Engng* **116**, 665–676.

Lyrintzis, A. & Mankbadi, R. R. 1995 On the prediction of the far-field jet noise using Kirchhoff's formulation. *AIAA Paper* 95-0508.

Mankbadi, R. R. 1990 The self-noise from ordered structures in a low Mach number jet. *Trans. ASME: J. Appl. Mech.* **57**, 241–246.

Mankbadi, R. R., Hayer, M. E. & Povinelli, L. A. 1994 Structure of supersonic jet flow and its radiated sound. *AIAA J.* **32**, 897–906.

Mankbadi, R. R. & Liu, J. T. C. 1984 Sound generated aerodynamically revisited: Large-scale structures in a turbulent jet as a source of sound. *Phil. Trans. R. Soc. Lond.* A **311**, 183–217.

Michalke, A. 1984 Survey on jet instability theory. *Prog. Aerospace Sci.* **21**, 159–199.

Mitchell, B. E., Lele, S. K. & Moin, P. 1995*a* Direct computation of the sound from a compressible co-rotating vortex pair. *J. Fluid Mech.* **285**, 181–202.

Mitchell, B. E., Lele, S. K. & Moin, P. 1995*b* The direct computation of the sound generated by subsonic and supersonic axisymmetric jets *Rep.* TF-66. Department of Mechanical Engineering, Stanford University.

Mitchell, B. E., Lele, S. K. & Moin, P. 1997 The direct computation of Mach wave radiation in an axisymmetric supersonic jet. *AIAA J.* **35**, 1574–1580.

Möhring, W. (1978) On vortex sound at low Mach number. *J. Fluid Mech.* **85**, 685–691.

Moin, P. & Mahesh, K. 1998 Direct Numerical Simulation: a tool in turbulence research. *Ann. Rev. Fluid Mech.* **30**, 539-578.

Moore, C. J. 1977 The role of shear-layer instability waves in jet exhaust noise. *J. Fluid Mech.* **80**, 321–367.

Morse, P. M. & Ingard, K. U. 1968 *Theoretical Acoustics.* Princeton University Press.

Myers, M. K. & Hausmann, J. S. 1990 On the application of the Kirchhoff formula for moving surfaces. *J. Sound Vib.* **139**, 174–178.

Pierce, A. D. 1989 *Acoustics: An Introduction to its Physical Principles and Applications.* Acoustical Society of America, New York.

Powell, A. 1964 Theory of vortex sound. *J. Acoust. Soc. Am.* **36**, 177–195.

Tam, C. K. W. & Hu, F. Q. 1989 On the three families of instability waves of high-speed jets. *J. Fluid Mech.* **201**, 447–483.

Thompson, J. F., Warsi, Z. U. A. & Mastin, C. W. 1985 *Numerical Grid Generation.* North-Holland.

Troutt, T. R. & McLaughlin, D. K. 1982 Experiments on the flow and acoustic properties of a moderate-Reynolds-number supersonic jet. *J. Fluid Mech.* **116**, 123–156.